Title

Identification and characterization of the dominant thermal resistance in lithium-ion batteries using operando 3-omega sensors

Journal

Journal of Applied Physics, 127(10)

ISSN

0021-8979

Authors

Lubner, SD
Kaur, S
Fu, Y
et al.

Publication Date

2020-03-14

DOI

10.1063/1.5134459

Peer reviewed

Identification and Characterization of the Dominant Thermal Resistance in Lithium-Ion Batteries using *Operando* 3-Omega Sensors

Authors: Sean D. Lubner[1], Sumanjeet Kaur[1], Yanbao Fu[1], Vince Battaglia[1], Ravi S. Prasher[1,2*].

***Correspondence to:** rsprasher@lbl.gov

Affiliations

[1] Energy Technologies Area, Lawrence Berkeley National Lab, 1 Cyclotron Road, Berkeley, CA, US, 94720

[2] Department of Mechanical Engineering, University of California, Berkeley, Etcheverry Hall, Hearst Ave #6141, Berkeley, CA 94720

Abstract

Poor thermal transport within lithium-ion batteries fundamentally limits their performance, safety, and lifetime, in spite of external thermal management systems. All prior efforts to understand the origin of batteries' mysteriously high thermal resistance have been confined to *ex-situ* measurements and without understanding the impact of battery operation. Here we develop a frequency domain technique that employs sensors capable of measuring the spatially resolved intrinsic thermal transport properties within a live battery while it is undergoing cycling. Our results reveal that the poor battery thermal transport is due to high thermal contact resistance between the separator and both electrode layers, and worsens as a result of formation cycling, degrading total battery thermal transport by up to 70%. We develop a thermal model of these contact resistances to explain their origin. These contacts account for up to 65% of the total thermal resistance inside the battery leading to far reaching consequences for the thermal design of batteries. Our technique unlocks new thermal measurement capabilities for future battery research.

Introduction

With the significant adoption of lithium (Li) ion batteries for applications ranging from electric vehicles to grid scale energy storage[1], it is clear that it will be very important to assure these batteries are safe and perform well. To this end, battery thermal management mitigates battery thermal runaway safety concerns, extends lifetime, reduces slow cold kinetics, and helps enable extreme fast charging[2–6]. So far the focus in the literature has primarily been on understanding thermal behavior of the external cooling system; however, there is a growing realization that understanding thermal transport inside the battery is vitally important to tackle the above-mentioned issues[5,7,8].

Because of the thin nature of battery layers (~20 μm – 70 μm) and their delicate electrochemical environment, most previous battery thermal transport studies[9,10] A) were performed *ex-situ* on deconstructed cells, B) lacked electrolyte, and C) were indirect, such as by stacking multiple copies of layers together but without resolving thermal contact resistances (*TCR*). Co-author Prasher in a previous study[8] found the cathode-separator *TCR* to be a significant thermal resistance, offering a clue to the reason for batteries' high thermal resistance, but they performed their measurements *ex-situ* and on isolated battery components without electrolyte. The absence of electrolyte can alter battery component thermal transport properties by a factor[11] of 2 to 3. They also did not investigate the separator's other (anode-facing) *TCR*. Gaitonde *et al.*[12] measured the separator-casing *TCR* and also found it to be an important thermal resistance impeding external thermal coupling to the battery, but this interface occurs only once, on the outside of the battery, whereas cathode/separator/anode interfaces repeat many times in the cell. Their measurements were also *ex-situ* and without electrolyte. No previous study has

been able to assess the TCR between each layer or do so *in-situ* in a full battery with its native environment including electrolyte.

This lack of *in-situ* experimentation has also precluded previous studies from investigating the effect of battery operation on local thermal properties. It is well known that cycling (both formation and during operation) changes the electrochemical behavior of batteries[13]. A natural question, then, is does cycling also change the thermal behavior of Li ion batteries? Answering this question necessitates *in-situ* and *operando* thermal measurements in the presence of electrolyte. In this work we report the first sensors capable of *operando* measurements of local thermal transport properties inside a Lithium-ion battery during formation cycling. We find the separator-anode and separator-cathode *TCR*s to be the primary sources of thermal resistance, which worsen as a result of formation cycling.

The rest of the paper is organized as follows. We first introduce the concept of the 3-omega technique, briefly derive its mathematical model, and describe the design of our samples and experiments. We then present the methodology and results of our *ex-situ* measurements of particular battery thermal properties that were lacking from the literature and necessary to analyze the data for our main *operando* 3-omega measurements. We then present the main results of this paper showing that separator-electrode *TCR* dominates battery internal thermal resistance. We then derive a mathematical model to explain the physics of the high *TCR* in batteries and discuss how it compares to and illuminates our results. We finish with some concluding remarks and future outlooks.

3-Omega Sensor Design

Operating Principle: In a unit cell of a battery there are five layers: the cathode, anode, separator, and two current collectors, each 10s of microns thick. For *operando TCR* measurements, thermal sensors must be minimally intrusive to the structure and functioning of the battery. Any steady state technique would require multiple internal temperature sensors spanning each interface plus a heater to supply controlled heating, leading to a very cumbersome and intrusive system. To circumvent this problem we used the transient 3-omega (3ω) technique[14,15], which is well-established for measuring the thermal conductivity (k) of bulk and microscale materials. The 3ω technique works by using an evaporated metal line to generate periodic surface heating at controlled frequencies and then detect the magnitude of the resulting temperature response on the sample's surface. The periodic surface heating produces a diffusive thermal wave that conducts into the bulk of the sample. The basic principle is shown in Figure 1(A). The biggest advantage of the 3ω technique is that the characteristic depth of the thermally probed region is defined by the thermal wave's "thermal penetration depth," $\delta_p = \sqrt{D/2\omega}$, where D is the sample's thermal diffusivity, and 2ω is the heating frequency of the thermal wave ($q = I^2R$ where q is the dissipated heat, so I at frequency ω produces heating at 2ω plus a DC offset). We deposit 3ω sensors on the battery's outer surface (Figure 1(B, C)) and control δ_p by adjusting ω to sweep the battery's full thickness from the top to the bottom layer. This allows us to non-invasively measure spatially resolved thermal transport properties of layers and interfaces during battery operation (Figure 1(D)). Incorporating sub-micron thickness 3ω sensors into a system with liquid, flexible, rough, porous, and corrosive components all under uniaxial compression poses significant fabrication challenges. We overcome these challenges using a multilayer thermally conducting and electrically insulating coating between the sensor and

current collector, and an electrolyte-resistant thermally insulating compressive foam over the top of the sensor. A second advantage (explained in greater detail in Appendix C: 3-Omega Measurements and Data Analysis) is an average signal-to-noise ratio (SNR) greater than 100, where here any thermal or electrical signal generated by the operation of the battery itself is also considered noise.

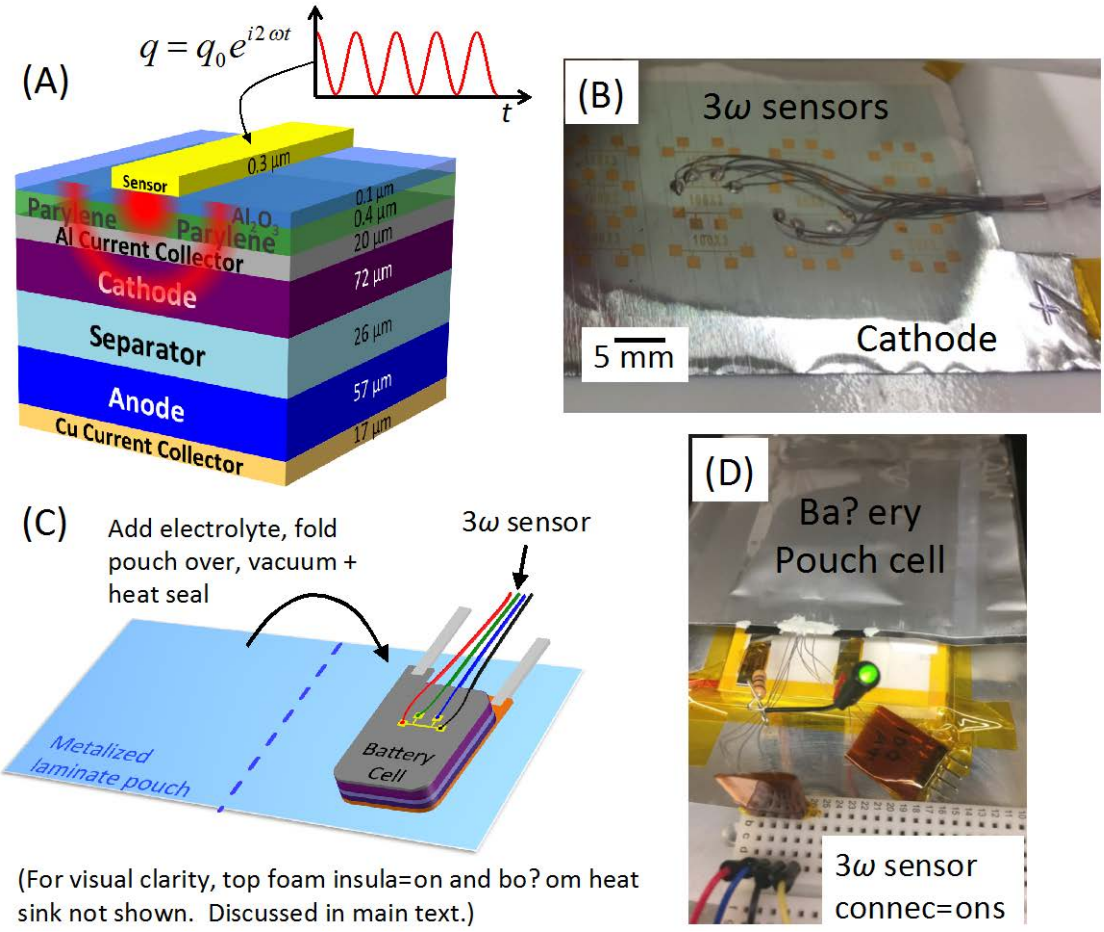

Figure 1. Preparation of battery samples with 3ω sensors. (A) Cutaway showing battery layers, thicknesses, sensor, and the diffusive thermal wave. The wave's penetration depth into the battery depends on its frequency. (B) Cathode with 300 nm Au 3ω heater line sensors deposited on top of 500 nm of electrical insulation. (C) Sensor-containing pouch cells are assembled inside a glove box where electrolyte is added and the pouch is vacuum-sealed. (D) *Operando* 3ω

thermal measurement on a battery pouch cell while it powers an LED (Note: most *operando* measurements were performed using a constant-current battery cycler, not an LED).

3-Omega Model: Our 3ω model is based on previously developed formulations in the literature[16–18] and is now briefly derived. We first follow Cahill[14] to develop an expression relating the thermal transfer function of the surface temperature responses from a periodic line source of heat to that of a finite width heat source that is experimentally measured by averaging over the width.

$$\frac{T_0}{q'} = \frac{1}{\pi}\int_0^\infty Z(m,\omega)\frac{\sin^2(mb)}{(mb)^2}dm \tag{1}$$

where T_0/q' is the frequency-domain spatially-averaged surface temperature response per unit heat per unit length of a finite width heater line, m is the integration variable and spatial Fourier transform variable perpendicular to the direction of the line of heat, ω is the electrical driving current frequency (half the heating frequency), b is the heater line half-width, and $Z(m,\omega)$ is the thermal transfer function relating the surface periodic temperature response to the surface periodic line source heating. Equation (1) here corresponds to Equation (8) in Ref[14].

Next, we follow Feldman[19] in developing an expression for the 1-D planar periodic heat source conduction through a multilayered stack. We note that an infinitely narrow (delta function) line source in real space is an infinitely spread out plane source in reciprocal space after Fourier transforming along the spatial dimension perpendicular to the line. Feldman's algorithm is 1D and hence requires plane sources of heat. We can therefore apply Feldman's algorithm in reciprocal space (1D heat flow) and plug the result into equation (1) to extend it to a finite width heater line, before inverse Fourier transforming back to real space. We have also

extended Feldman's solution from a thermally isotropic to an anisotropic material. The final expression for the experimentally measured frequency-dependent and spatially-averaged heater line temperature is

$$T_0(\omega) = \frac{q'}{\pi}\int_0^\infty \frac{B_1^+(m)+B_1^-(m)}{B_1^-(m)-B_1^+(m)}\frac{\sin^2(mb)}{\gamma_1(mb)^2}dm$$

$$\begin{pmatrix} B_1^+ \\ B_1^- \end{pmatrix} = \left(\prod_{n=1}^{n=N} U_n \Gamma_{n,n+1}\right)\begin{pmatrix} 0 \\ 1 \end{pmatrix}$$

$$U_n = \begin{bmatrix} e^{-u_n L_n} & 0 \\ 0 & e^{u_n L_n} \end{bmatrix} \qquad (2)$$

$$\Gamma_{n,n+1} = \frac{1}{2\gamma_n}\begin{bmatrix} \gamma_{n+1}+\gamma_n & \gamma_n-\gamma_{n+1} \\ \gamma_n-\gamma_{n+1} & \gamma_{n+1}+\gamma_n \end{bmatrix}$$

$$\gamma_n = k_{n,cross\,plane}u_n = k_{n,cross\,plane}\sqrt{\frac{k_{n,in\,plane}}{k_{n,cross\,plane}}m^2 + \frac{i2\omega}{D_{n,cross\,plane}}}$$

where T_0 now gives the frequency-domain surface temperature response to the periodic heating (at frequency 2ω) from a width $2b$ heater line on top of a multilayered stack, measured by averaging the temperature across the width (because in practice the temperature is measured from the spatially averaged electrical resistance of the sensor). N is the total number of layers in the stack, with the top layer being layer 1 (the outside environment such as air is layer 0) increasing to layer N at the bottom of the stack, k, L, and D are the thermal conductivity, thickness, and thermal diffusivity of each layer, respectively, and subscripts denote layer number. "In plane" and "cross plane" subscripts denote the diagonal thermal conductivity tensor component corresponding to thermal transport within the plane or perpendicular to the plane of

the battery layers. All other undefined variables are the same as in Equation (1). Equation (2) gives the complete thermal domain solution for the periodic average surface temperature response with all expressions defined.

In order to relate T_0 to experimentally measured values, we follow Dames and Chen[15] in relating the thermal domain transfer function to the experimentally measured electrical domain transfer function by means of the temperature coefficient of resistance (α).

$$V_{3\omega} = -\frac{1}{2}\alpha R_0^2 I^3 \left[\mathrm{Re}\left\{\frac{T_0}{q}\right\} + i\,\mathrm{Im}\left\{\frac{T_0}{q}\right\} \right] \tag{3}$$

where $V_{3\omega}$ is the measured third harmonic voltage drop across the heater line, α is the temperature coefficient of resistance, I is the electrical current, q is the total heat [W] dissipated by the sensor of length l, and T_0 is the complex frequency-dependent temperature defined by Eq. (2). Re{} and Im{} denote the real and imaginary components (corresponding to in-phase and out-of-phase signal response components). All quantities are root-mean-square (RMS). This final expression is what is used in data fitting, as $V_{3\omega}$ is the experimentally measured quantity.

Sensitivity Analysis and Optimization of Sample Design: In our experiments we are interested in measuring the total thermal contact resistance of both separator-electrode interfaces, $TCR_{s\text{-}e}$ (i.e. $TCR_{s\text{-}e} = TCR_{separator\text{-}cathode} + TCR_{separator\text{-}anode}$). We therefore use the above model to perform extensive sensitivity calculations to optimize the design of our experiments in order to simultaneously maximize sensitivity to $TCR_{s\text{-}e}$ while minimizing sensitivity to difficult-to-quantify variable external environmental factors. Our final optimized experiment and sample designs are shown in Figure 2. Full details of the sensitivity analysis are given in Appendix A: Optimization of Sample Design, and details of the electrochemistry, battery materials, and

fabrication process are given in Appendix B: Sample Fabrication. We ensure that >99% of the sensor's heat conducts down through the battery cell.

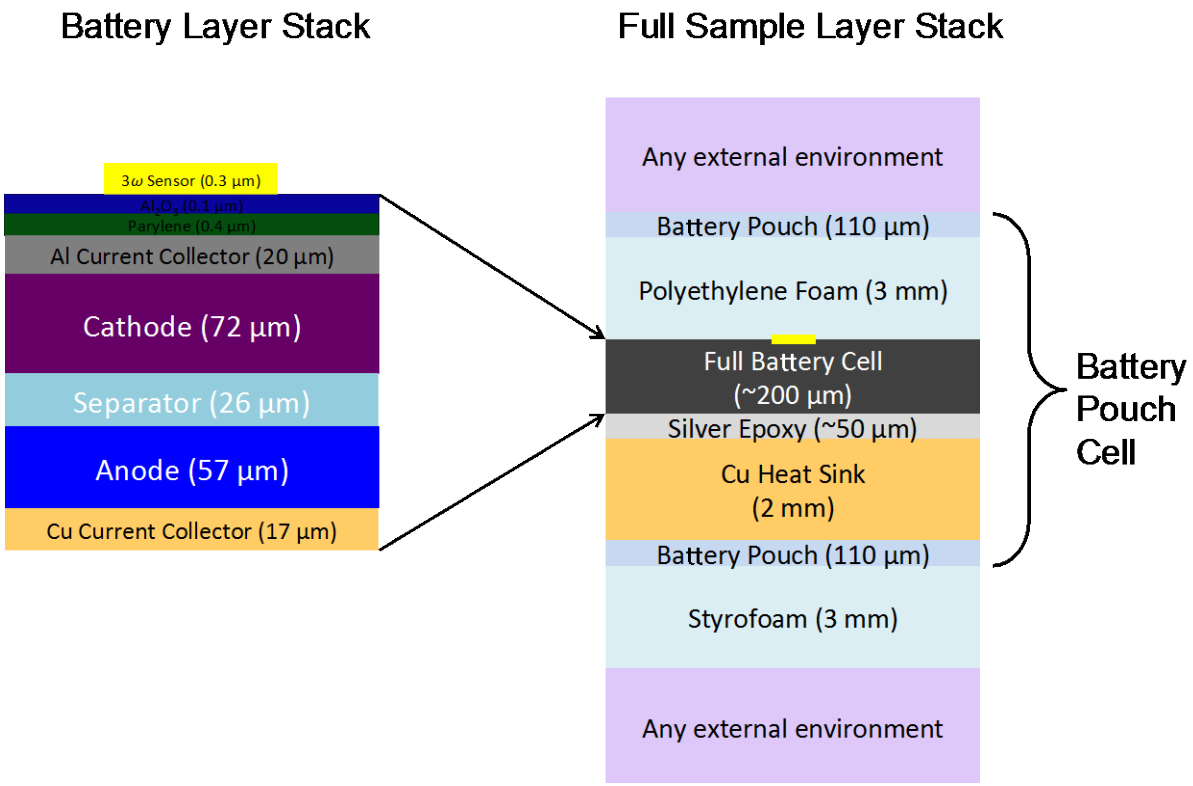

Figure 2. Full sample layer stack geometry. Based on sensitivity studies, an optimal sample design is created with layers placed outside the battery cell to maximize the thermal signal to the battery layer interfaces while eliminating thermal sensitivity to any external environment outside the battery pouch cell.

Data Analysis: We simultaneously fit two free parameters in the model. The first fitted parameter is the unknown thermal resistance of the parylene electrical insulation layer, $R_{parylene} = L_{parylene}/k_{parylene}$, and the second parameter is the total thermal contact resistance of the two separator-electrode interfaces, $TCR_{s\text{-}e}$ (i.e. $TCR_{s\text{-}e} = TCR_{separator\text{-}cathode} + TCR_{separator\text{-}anode}$). These two parameters affect the surface temperature response in qualitatively different ways and can be

robustly fit simultaneously. Full details are given in Appendix C: 3-Omega Measurements and Data Analysis.

Ex-Situ **Characterizations**

Ex-Situ Electrode Thermal Conductivity Measurements: Literature values for the cross-plane thermal conductivity of dry and wet anodes and cathodes are sparse and inconsistent, sometimes varying by an order of magnitude (see, for example, Ref[10] versus Ref[20]). Such uncertainty in these input parameters for our 3-omega model would make effective data analysis impossible for the battery measurements. Therefore, we directly measure *k* of our electrodes *ex-situ* in-house using a variant of the linear heat flow Cut Bar method[21]. Our Cut Bar system is shown in Figure 3(A). Heat flows from the heater on top, down through the 1" x 1" copper bars and is dissipated passively through the large thermal mass metal base into the metal optical table lab bench and environment. During measurements, a sample is sandwiched between the two copper bars such that the 1D heat flow passes through it. A series of 4 thermocouples each in the top and bottom bar measure the bars' internal temperatures. Approximately 1 inch of fiberglass insulation wraps all around the apparatus during measurement for thermal isolation from the environment. Our simulations showed that for our samples a guard heater around the outside of this insulation is not needed. The thermocouples were calibrated by applying a thin layer of highly thermally conducting grease between the copper bars in place of the sample, wrapping the system in thermal insulation, and turning off the heating. The resulting Biot number is ~10^{-5} (very isothermal) and the thermocouples are then calibrated to all read the same temperature.

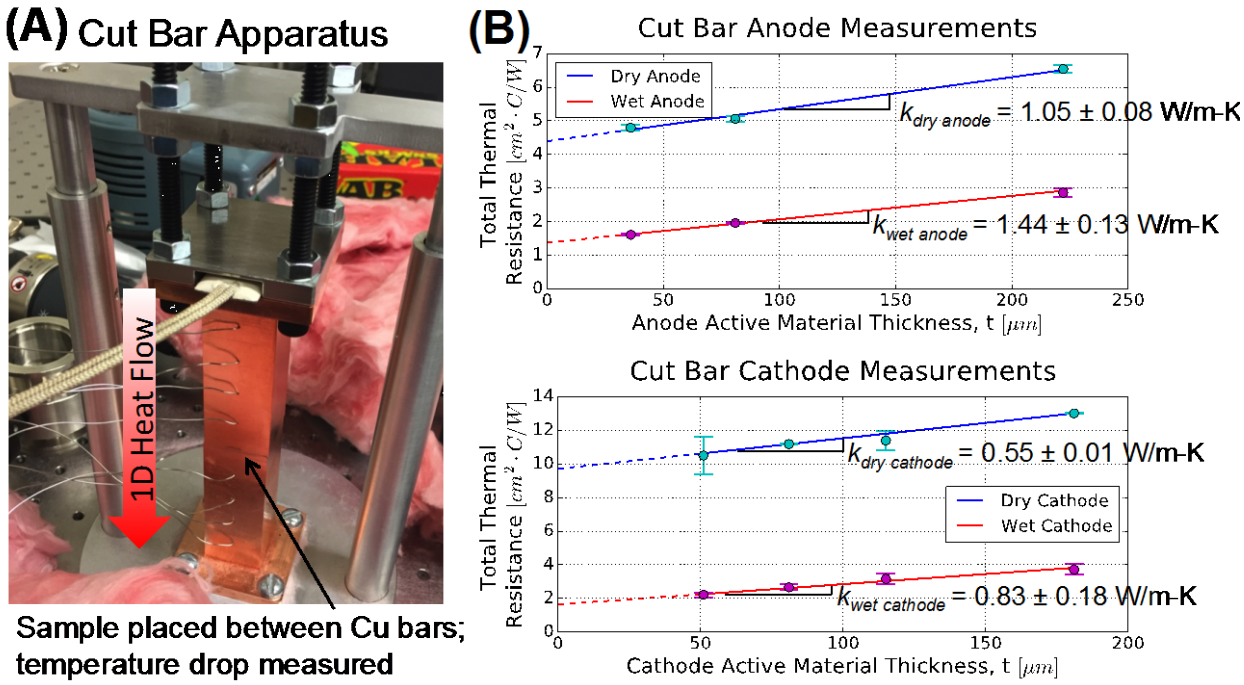

Figure 3. Linear heat flow Cut Bar apparatus for measuring thermal conductivity of individual electrodes. (A) a picture of the Cut Bar showing the copper bars fitted with thermocouples. Heat flows down from the heater on top and is dissipated through the large thermal mass metal base into the metal optical table lab bench and environment. (B) Results of all Cut Bar measurements on wet and dry cathodes and anodes. Error bars show one standard deviation from 2 to 4 repeated measurements. The thermal conductivity can be extracted from the slope of the total thermal resistance vs. electrode active material thickness, separating out all thermal contact resistances.

The measurement is run until steady state is reached, taking anywhere from 2 to 6 hours, depending on whether it is immediately following a previous measurement. Once steady state is reached, the measurement is allowed to run for an additional few hours. The recorded temperature gradients are averaged over these final few hours and are typically stable to less than 0.5% fluctuation. The temperature gradient in the bottom bar is recorded from the thermocouples, from which the heat flux, *Q*, is calculated from the known copper thermal conductivity. A typical heat flux used is 12 Watts (for the 1" x 1" cross sectional area), resulting

in a temperature drop of approximately ΔT = 20 K across the sample. The temperature gradient in each bar is used to extrapolate to the bar surface and calculate this total temperature drop, ΔT, across the sample. The total thermal resistance of the sample + contact resistances is then calculated from $R_{thermal} = \Delta T/Q$. For wet samples, electrodes were soaked in a delithiated electrolyte solvent (the same composition as the electrolyte used in the batteries except without any lithium salt added). A single layer of Kapton tape was then placed around the perimeter of the bars encompassing the sample, forming a watertight seal to prevent evaporation during the measurement. This layer of tape introduces negligible parasitic heat pathways.

The total thermal resistance measured by the Cut Bar can be expressed as

$$R_{therm,total} = TCR_{bar-CC} + \frac{L_{CC}}{k_{CC}} + \frac{L_e}{k_e} + TCR_{e-bar} \tag{4}$$

where $R_{bar\text{-}CC}$ and $R_{e\text{-}bar}$ are the thermal contact resistances between the copper bar and current collector, and the copper bar and electrode, respectively. Subscript *CC* refers to current collector and subscript *e* refers to electrode active material. By varying the thickness of the electrode active material, L_e, we can isolate the thermal conductivity of the electrode.

$$\frac{\partial R_{therm,total}}{\partial L_e} = \frac{1}{k_e} \tag{5}$$

We thus fabricate electrodes of varying active material thicknesses and measure their total thermal resistances using the Cut Bar. We then calculated the single electrode active material *k* from the slope of total thermal resistance versus material thickness, as shown in Figure 3(B). This approach of calculating *k* is more accurate than trying to directly subtract out each additional term in Equation (4). The latter approach tries to subtract several large numbers from another large number in order to back out a small number, and hence is prone to large errors.

We note that to our knowledge these are the first direct measurements of individual electrode active material cross-plane thermal conductivities. The final fitted values for *k* of our dry and wet anode and cathode are given in Figure 3(B).

Ex-Situ Electrode Thermal Contact Resistance Measurements: Although prone to larger uncertainties as mentioned above, the approach of subtracting out each individual thermal resistance to isolate a single desired thermal resistance in a Cut Bar measurement can be used when trying to measure the largest contributor to the total thermal resistance. Figure 4 shows the setup for a series of Cut Bar measurements used to measure the dry and wet *TCR* between the electrodes and the smooth copper bars. Although less representative than the *operando* 3ω measurements, this more controlled *ex-situ* approach enables us to cleanly separate out the relative magnitude of the cathode and anode *TCR*s by creating a system that has only one or the other type of interface.

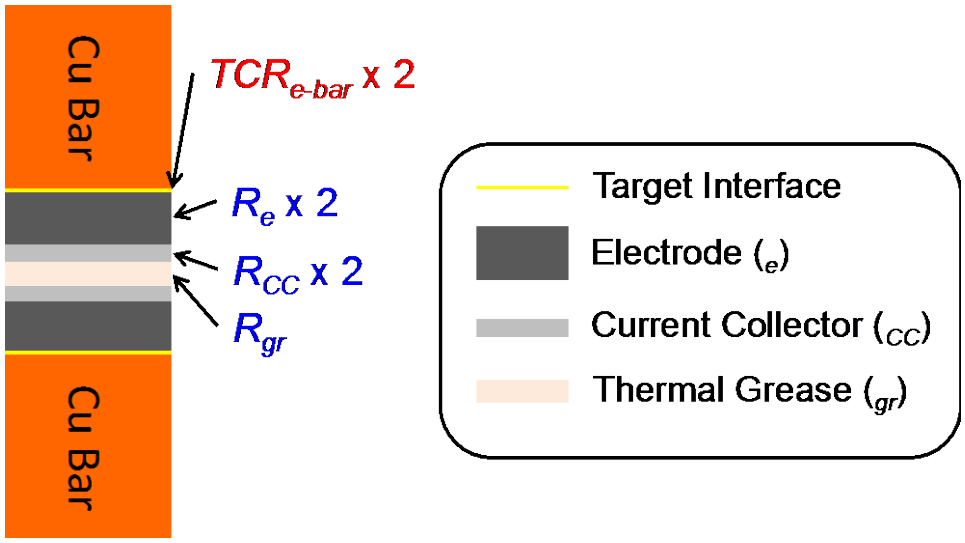

Figure 4. *Ex-situ* Cut Bar measurements of electrode-Cu bar thermal contact resistance ($TCR_{e\text{-}bar}$). The already known material thermal resistances are shown in blue. The unknown thermal resistance is shown in red, and is calculated by subtracting out all other known resistances from

the total measured thermal resistance. The same process is repeated for cathode and for anode, with and without electrolyte.

Cut Bar measurements were repeated on samples as shown in Figure 4 both with and without electrolyte, and with only one type of electrode (anode or cathode) present at a time. The contributions from the electrode bulk material, current collectors, and thermal grease were subtracted from the total thermal resistance. The left over thermal resistance is the sum of two thermal contact resistances between the electrode and the copper bar, and dominates the total thermal resistance in all cases.

From this procedure we measure the following single-interface resistances:

- $TCR_{anode\text{-}copper,\ dry} = 2.28 \pm 0.22$ cm^2-C/W
- $TCR_{anode\text{-}copper,\ wet} = 0.77 \pm 0.04$ cm^2-C/W
- $TCR_{cathode\text{-}copper,\ dry} = 4.84 \pm 0.07$ cm^2-C/W
- $TCR_{cathode\text{-}copper,\ wet} = 1.17 \pm 0.14$ cm^2-C/W

Note that *TCR* for anode and cathode are of comparable magnitude (within a factor of 2). *TCR* uncertainties are calculated by propagating the individual uncertainties (from literature or 2 to 5 independent measurements) of the input parameters. These input parameters include the thickness and thermal conductivity of the current collectors, thermal grease, and electrode active material.

Results

Two separate battery pouch cells were successfully fabricated with intact 3ω sensors and measured (details given in Appendix B: Sample Fabrication). The thermal transport properties

of the batteries were measured periodically during their formation charge/discharge cycles until the sensors broke after one to two weeks (note: it is not possible to put sensors outside the pouch due to low sensitivity through the pouch). The sensors lasted up to 6 cycles and we are in the process of improving the sensor design to last longer for future measurements. Complete details of the measurement protocol are given in Appendix C: 3-Omega Measurements and Data Analysis. We measure the combined thermal contact resistance of both separator-electrode interfaces, $TCR_{s\text{-}e}$ (i.e. $TCR_{s\text{-}e} = TCR_{separator\text{-}cathode} + TCR_{separator\text{-}anode}$). The results of all 3ω measurements are summarized in Figure 5.

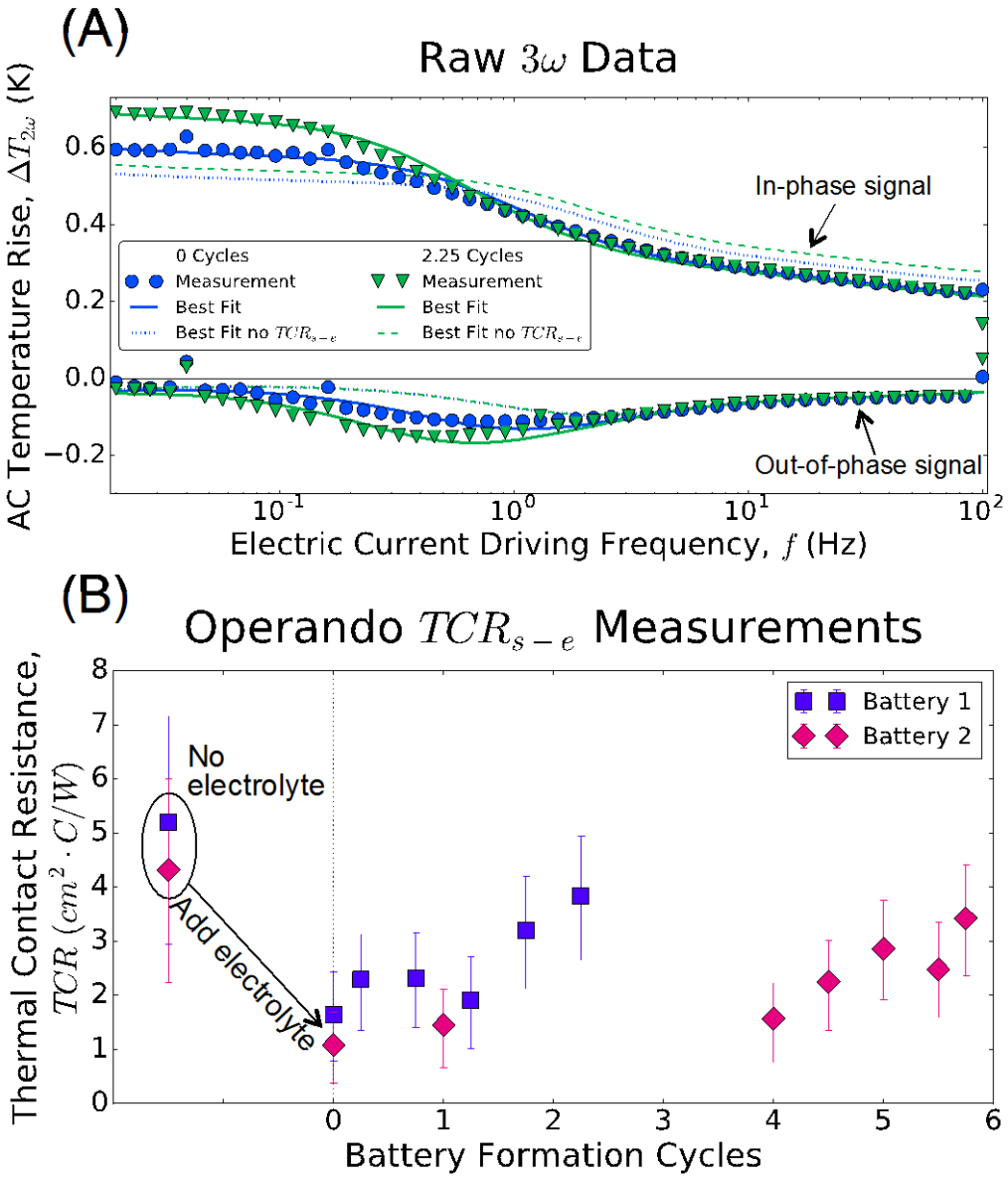

Figure 5. Raw and analyzed 3ω data during battery formation cycles. (A) Representative raw 3ω data (Battery 1) before and after 2.25 formation cycles, showing the change in $TCR_{s\text{-}e}$ due to formation cycling and showing that it is not possible to fit the data without including $TCR_{s\text{-}e}$. (B) Total combined thermal contact resistance from both separator-electrode interfaces ($TCR_{s\text{-}e}$) measured in live batteries as they undergo formation cycles. Measurements performed after fractional numbers of cycles were performed *operando* during charging or discharging. Points before "0 Cycles" are dry (i.e. before electrolyte was added). Data ends where sensors broke. Error bars show the 95% confidence interval calculated from Monte Carlo simulations, explained in **Appendix D: Statistical Analysis**.

Figure 5(A) shows representative raw 3ω data and accompanying data fitting for one pouch cell immediately after assembly and again after two and a quarter battery formation cycles, showing the change in raw data as the $TCR_{s\text{-}e}$ increases. Figure 5(B) shows that the $TCR_{s\text{-}e}$ continues to increase over time with formation cycling. Figure 5(A) also shows that it is not possible to accurately fit the data unless we allow for a $TCR_{s\text{-}e}$ in our thermal model. The dashed lines show the best possible fit that can be achieved for the data if omitting the existence of the $TCR_{s\text{-}e}$. The dashed lines overlap for the out-of-phase signal before and after cycling (note: including k_{anode} or $k_{cathode}$ as an additional fitting parameter in place of $TCR_{s\text{-}e}$ results in unphysically low fitted values and still a poor fit). Figure 6(A) shows the relative contribution of each battery component to the total battery thermal resistance at the end of formation cycling for the same raw data plotted in Figure 5(A). The $TCR_{s\text{-}e}$ accounts for 65% of the battery's total internal thermal resistance for both batteries measured. Before formation cycling, the $TCR_{s\text{-}e}$ in the just-assembled batteries accounted for 36% to 45% of the total internal thermal resistance (still the largest single contributor among all components and interfaces). Figure 6(B) shows the representative voltage traces for three cycles (battery 2) while the battery periodically underwent 3ω measurements, showing normal behavior of the battery, unaffected by the presence of our sensors.

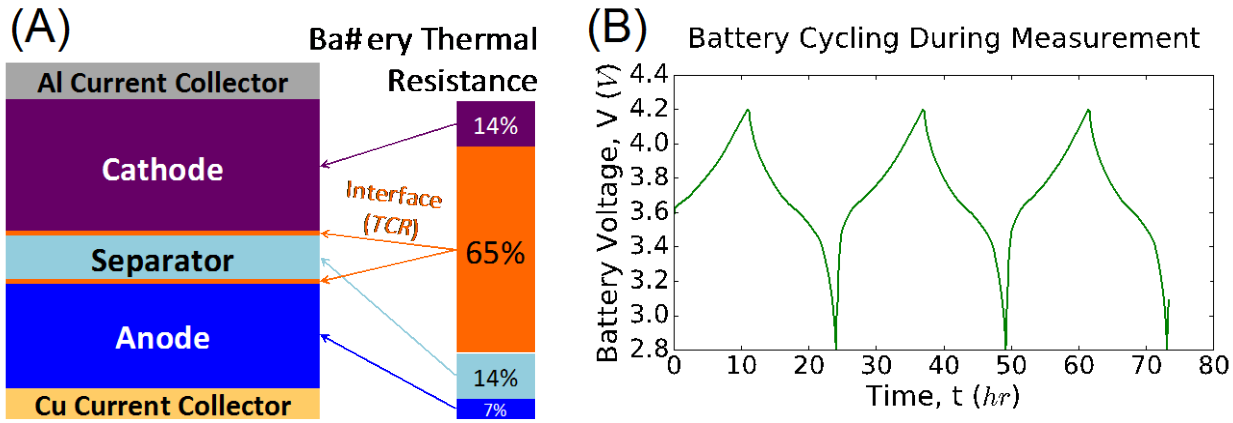

Figure 6. (A) Relative contribution of each component of the battery unit cell to the total cross-plane thermal resistance after formation cycling (Battery 1; post-cycling). Before formation cycling, $TCR_{s\text{-}e}$ accounted for 45% (Battery 1) and 36% (Battery 2) of the total just-assembled battery thermal resistances. (B) Representative battery formation charging/discharging cycles while thermal 3ω measurements were performed, demonstrating normal electrochemical behavior (Battery 2).

Thermal Contact Resistance Model

To understand the origin of this high *TCR* we develop a model for the *TCR* between the electrode and a deformable flat surface based on previous work by Prasher[22]. Figure 7(A) shows the setup for our *TCR* model while Figure 7(B) shows the microscale structure of the battery electrodes and separator. We treat the interface as a sheet of idealized deformable spherical particles (radius r_p) being pressed into a deformable flat substrate in the presence of an interstitial fluid (either air or liquid electrolyte). The interface resistance of the solid originates from the constriction resistance (R_c) due to constriction of heat flux lines and due to phonon acoustic mismatch at the boundary (R_b). As shown in the thermal network in Figure 7(A), heat also flows in parallel through the interstitial fluid (R_f).

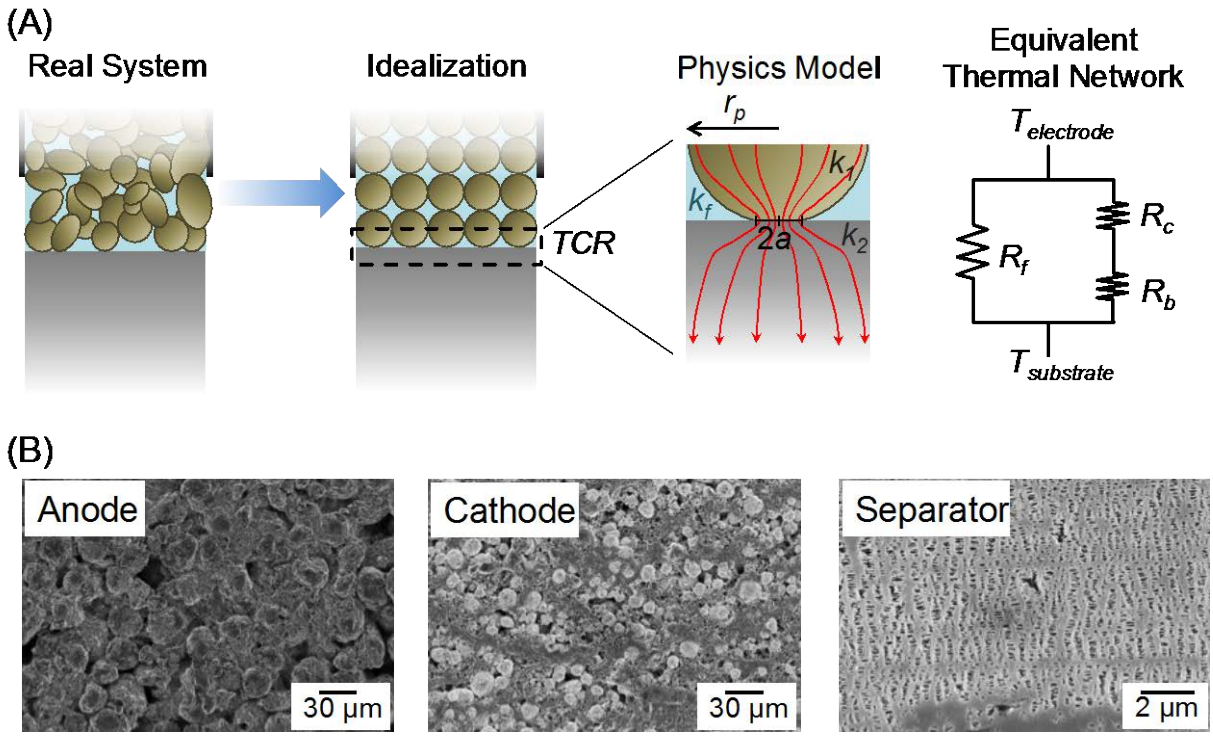

Figure 7. Thermal model for the thermal contact resistance (*TCR*). (A) Theoretical idealization of a real polydisperse, porous, composite electrode in contact with a deformable flat substrate. The bulk of the electrode above the interface is treated as a homogenous medium with a single effective *k*. Within the interfacial region, heat passes in parallel through the fluid (R_f) while heat flux lines are constricted (R_c) through nanoscopic contact points and only some phonons transmit through the boundary (R_b) due to acoustic mismatch between dissimilar materials, leading to an overall macroscopic thermal contact resistance between the two battery layers. (B) Scanning electron microscope (SEM) images of the porous battery separator, anode, and cathode.

Heat flux lines flowing through the solid particles are constricted as they pass through the small contacting area (radius $a << r_p$). This constriction resistance (R_c) offers the primary thermal resistance at the interface. The constriction radius, *a*, is calculated based on the 5 PSI of applied pressure and the mechanical properties of the materials involved. We follow Ref[22] and apply a Hertzian contact analysis yielding $a = \left(0.75Fr_p/E^*\right)^{1/3}$, where *F* is the force per particle, r_p is the particle radius, and $E^{*-1} = \frac{1-\nu_1^2}{E_1} + \frac{1-\nu_2^2}{E_2}$, where *E* is the Young's modulus and *v*

is the Poisson's ratio. Subscript 1 denotes the particle and subscript 2 denotes the deformable flat substrate. For a simple cubic packed layer of spherical particles (square lattice of periodicity $2r_p$) assuming only a fraction θ of them make contact with the substrate, the force per particle is $F = (2r_p)^2 P/\theta$, where P is the average downward pressure being applied to the electrode. This comes from calculating the average force per particle-occupied lattice site required to balance the applied pressure in static equilibrium. For our system this external pressure dominates and internal van der Waals adhesive forces are neglected. An approximate average particle radius of 10 μm is used to model both the anode and cathode, based on the SEM pictures shown in Figure 7(B). While the cathode particles are on average smaller than the anode particles, they also have relatively flat regions between particles corresponding to an effectively much larger radius. These effects are averaged when modeling the cathode as an idealized layer of densely packed and identically sized particles. From the constriction radius, the thermal constriction resistance per particle is calculated according to[23] $R_c = \frac{1}{4k_1 a} + \frac{1}{4k_2 a}$, where k_1 and k_2 are the thermal conductivities of the particle and substrate, respectively. In each case, we calculate k_1 by applying the Bruggeman model[24] to our measurements of k of the electrolyte (measured in-house using a commercial 2200 Hot Disk purchased from *Thermtest* based on the transient plane source technique[25]) and of the wet and dry electrodes from the *ex-situ* measurements.

Additionally, there is a boundary resistance (R_b) between the particle and the substrate because the heat-carrying phonons in the electrode particles transmit with <100% probability into the substrate. This results from the mismatch between the acoustic vibrational spectra of the two materials. We used an approximate average value of R_b" = 10^{-8} m^2-K/W based on typical values for solid-solid thermal boundary conductances where heat transport in at least one of the

solids is phonon dominated[26]. R_b acts only at the points where both materials are in direct contact, and so only acts over the constriction area. Therefore the thermal boundary resistance per particle is given by $R_b = R_b^{"}/(\pi a^2)$. R_c is a much stronger effect than R_b for all systems (by a factor of 10 to 1000).

As shown in the thermal network in Figure 7(A), heat flows in parallel through the interstitial fluid (R_f). R_f is derived from the total thermal resistance of the fluid-filled interstitial space between particles for simple cubic packed spheres (Figure 8). For a lattice site where a particle is contacting the substrate, R_f can be calculated by summing up the series differential thermal resistances of each thin slice perpendicular to the direction of heat flow (Figure 8(D)). The resulting integral yields $R_f = \int \frac{dx}{k_f A_f} = \frac{1}{k_f \pi r_p^2} \int_{x=0}^{r_p} \frac{dx}{\left(\frac{4}{\pi}-1\right)+\left(\frac{x}{r_p}\right)^2} \approx \frac{0.663}{k_f r_p}$, where k_f is the thermal conductivity of the fluid and A_f is the cross sectional area of the fluid a distance x from the middle of the spherical particle. R_f gives the thermal resistance of the fluid surrounding each contacting particle. Convection effects are negligible for interstitial spaces this small.

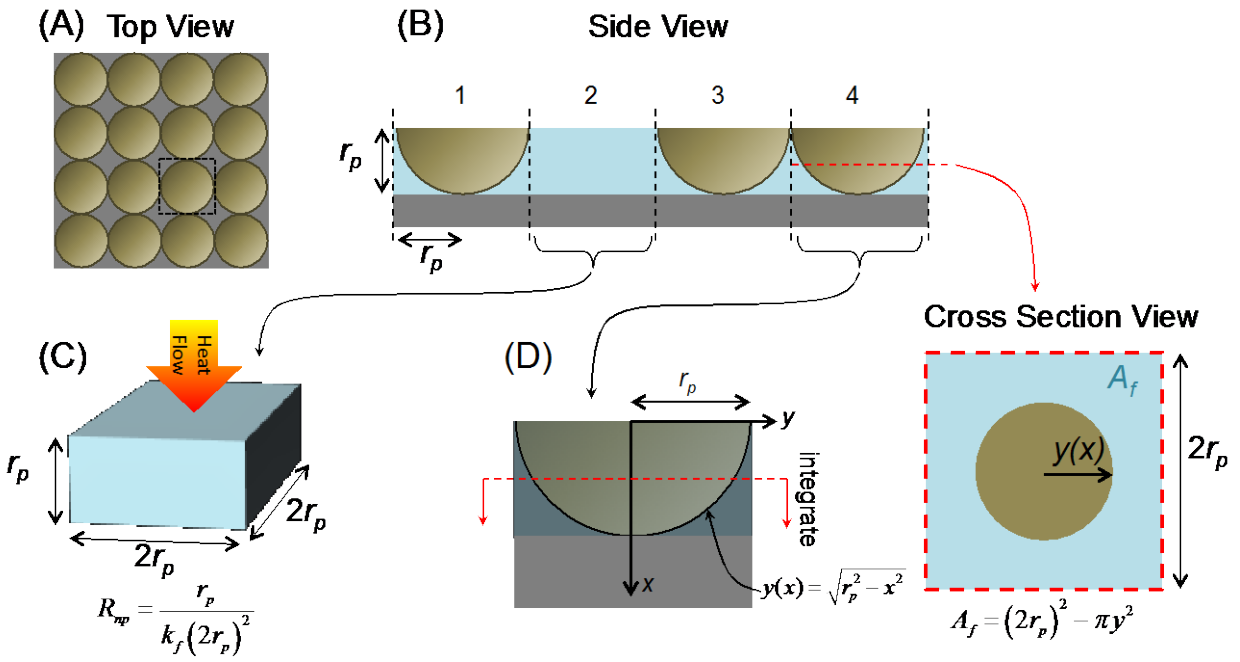

Figure 8. Fluid resistances in the *TCR* model. (A) Top view of idealized cubic lattice of spherical particles on a flat substrate. Dashed-line square indicates one lattice site. (B) Side view of lowest layer of particles in contact with flat substrate with interstitial fluid for the case of $\theta = 0.75$. There is no particle contacting the substrate at lattice site 2, so heat conduction is just through the fluid. (C) The thermal resistance for a lattice site with no contacting particle is just a linear heat conduction resistance through the fluid, $R = L/kA$, where L is the thickness in the direction of heat flow and A is the cross sectional area perpendicular to the direction of heat flow. (D) We calculate the conduction resistance through the fluid around the particle by taking differential thermal resistances for each horizontal slice, $dR = dx/k_f A_f$, and integrating them along the direction of heat flow.

Real electrodes and substrates are not perfectly flat. Therefore, for any given square lattice site in the idealized layer of simple cubic packed particles at the interface shown in Figure 7(A), that lattice site's particle can either be in contact with the substrate or not be in contact (Figure 8(B)). The fraction of particles in contact is given by θ. If the particle is in contact, then that lattice site's total thermal resistance for the contacting particle (R_p) is the combination of the fluid resistance (R_f) in parallel with the sum of the constriction and boundary resistances (R_c +

R_b), namely $R_p = \left(\frac{1}{R_f} + \frac{1}{R_c+R_b}\right)^{-1}$. If the particle is not in contact, then the thermal resistance for that lattice site is taken to be the thermal resistance of a layer of fluid of equal thickness (r_p) but without a particle present (Figure 8(C)). Specifically, the thermal resistance for a square lattice site with no particle is $R_{np} = 1/(4k_f r_p)$, which should not be confused with the similar expression for R_c (which has a in place of r_p).

The thermal resistance from each site in the idealized lattice adds in parallel with the thermal resistance at every other lattice site. Given that a fraction θ of the particles are in contact and each lattice site has an area of $4r_p^2$, the total predicted thermal contact resistance is therefore

$$TCR = \frac{4r_p^2}{\frac{\theta}{R_p} + \frac{1-\theta}{R_{np}}} \tag{6}$$

Equation (6) is the final expression used to predict the total net thermal contact resistance between an electrode and a flat surface being pressed together. An approximate middle ground value of $\theta = 0.5$ is used from considering the SEM pictures (Figure 7(B)). The precise value of θ has a small effect on the results because there is still heat conduction through fluid wherever a lattice site has no particle making contact. Compared to our choice of $\theta = 0.5$, the limiting case values of $\theta = 0$ and $\theta = 1$ only change the total predicted separator-electrode *TCR* by approximately 40% for wet contacts and 20% for dry contacts. Because the nano-sized pores in the separator are much smaller than a the separator is treated as a single homogeneous material with effective thermal and mechanical properties. These properties, along with all other thermophysical properties used in applying equation (6), are listed in Table 3 in Appendix E: Thermophysical Properties for Thermal Contact Resistance Model.

Discussion

The predictions of our *TCR* model compared with all *TCR* measurements are summarized in Figure 9. This includes dry and wet, *ex-situ* and *operando*, and electrode-copper and electrode-separator measurements. Good agreement is observed between prediction and experiment for all measurements. The physical reason for the increase in $TCR_{s\text{-}e}$ with cycling is unknown, so we cannot yet include it in our *TCR* model. Therefore, for $TCR_{s\text{-}e}$ measurements in Figure 9 we only compare our model's predictions with the just-assembled pouch cell data before any cycling. For all systems, the dry *TCR* is higher than the wet *TCR*. This results from the lower thermal conductivity of air (k_{air} = 0.025 W/m-K) filling the inter-particle spaces in dry electrodes as compared to electrolyte ($k_{electrolyte}$ = 0.2 W/m-K) in wet electrodes. The cathode-copper *TCR* is greater than the anode-copper *TCR* because the NMC active particles in the cathode are both harder (E_{NMC} = 199 GPa) and have a lower thermal conductivity (k_{NMC} = 2.3 W/m-K) than the graphite active particles ($E_{graphite}$ = 32 GPa; $k_{graphite}$ = 5.8 W/m-K) in the anode. The NMC particles therefore deform less, resulting in smaller constriction contact radii (a) between cathode particles and copper than anode particles and copper, and hence higher *TCR*. This difference between anode and cathode *TCR* reduces for wet contacts because more of the heat flows through the electrolyte, which is the same for both anode and cathode. For the 3-omega pouch cell *TCR* measurements Figure 9 shows the total combined $TCR_{s\text{-}e}$ to better facilitate comparison with experiments, because the 3-omega measurements lack sufficient precision to separate out the cathode-separator versus anode-separator *TCR* across the 26 μm thick separator and only measure their combined value. However, the *TCR* model predicts the cathode-separator and anode-separator *TCR*s to be nearly identical for both the dry and wet case. This is due to the

very soft and compliant separator ($E_{dryseparator}$ = 0.21 GPa; $E_{wetseparator}$ = 0.18 GPa) dominating the deformation mechanics and causing the restriction contact radii to be much larger and equal for both electrodes. This effect dominates over the different particle thermal conductivities. Thus both the top and bottom separator interfaces have approximately equal contributions to the battery's total cross-plane internal thermal resistance.

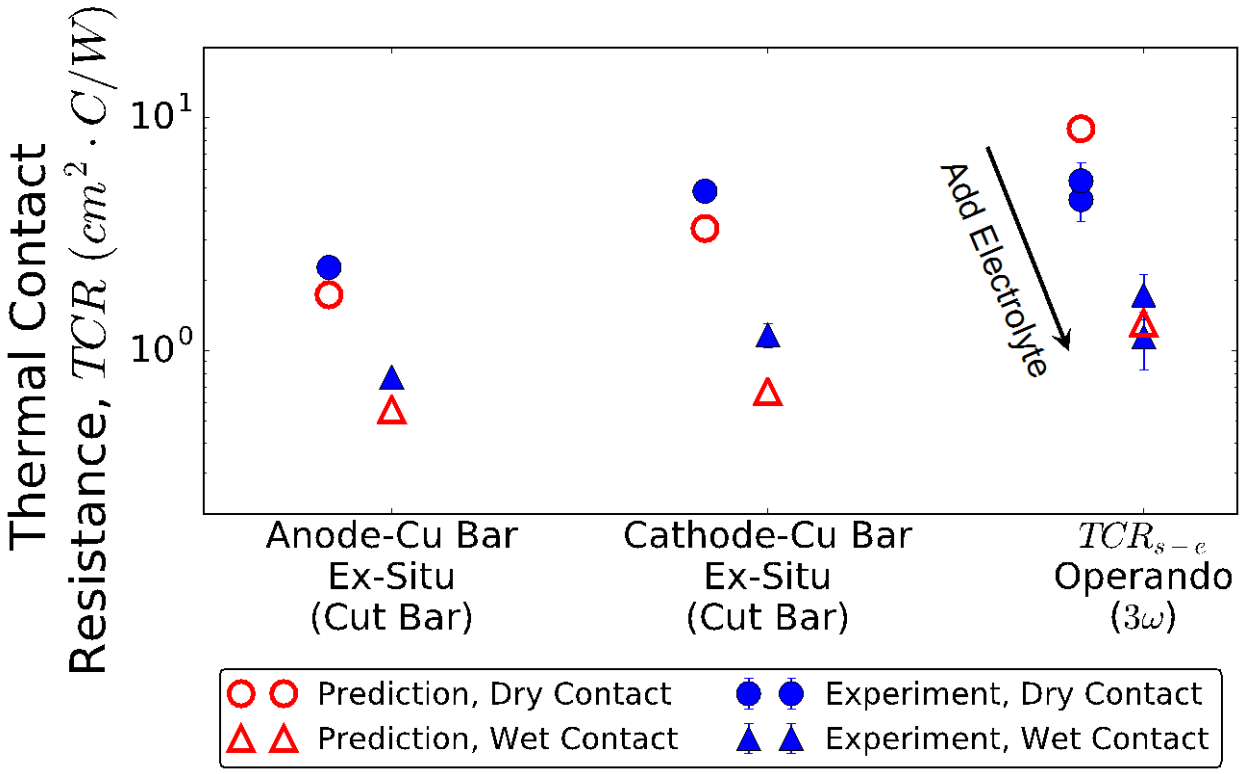

Figure 9. Predictions of our *TCR* model (red hollow points) for dry (circles) and wet (triangles) contacts compared to experimental measurements (blue filled-in points) from *ex-situ* cut bar measurements (copper-electrode *TCR*) and *operando* 3ω measurements (separator-electrode *TCR*).

The *TCR* model predicts that inside the battery the heat path through the particles is 2 to 3 times more thermally resistive than the heat path through the electrolyte. For dry cells the heat path through the air and through the solid particles have similar thermal resistances. As a consequence the model predicts the best ways to reduce the $TCR_{s\text{-}e}$ are to increase k of the electrolyte or reduce the electrode particle sizes (because the increased number of thermal conduction pathways per unit area out-weighs the decreased thermal conductance per particle contact). This can be intuitively understood as approaching the limit of two perfectly smooth contacting surfaces as particle size shrinks to zero. Interestingly, changing the applied external pressure, changing the fraction of contacting particles at the separator-electrode interface, or changing k of any other material all have relatively small effects on $TCR_{s\text{-}e}$ in this regime.

The *operando* sensors offer the uniquely ability to observe that the $TCR_{s\text{-}e}$ worsens during the formation cycling (Figure 5(B)). While we cannot say at this time why this happens, we can speculate on the most likely possible explanations. First, to verify that the change in data with cycling is due to the $TCR_{s\text{-}e}$ and not changes in other parts of the battery, we attempted to fit the post-cycling 3ω data while allowing the k of the cathode or anode to vary instead of the $TCR_{s\text{-}e}$. Such attempts either resulted in unphysically low fitted thermal conductivities (e.g. less than half the thermal conductivity of the fully dry electrode), or entirely failed to fit the data. We also attempted 3- and 4-parameter fits allowing the thermal conductivities of one or both electrodes to vary simultaneously with the $TCR_{s\text{-}e}$ and parylene thermal resistance. In most cases these attempts also resulted in unphysical thermal conductivities for the electrodes or entirely failed to fit the data. In the successful attempts, the fitted values for the electrodes and $TCR_{s\text{-}e}$ agreed to better than 5% with the values obtained from the 2-parameter fit that attributed all change to the

$TCR_{s\text{-}e}$. Because some fitting attempts failed, we cannot entirely rule out the possibility of some change being due to varying electrode properties, and future work is still needed to confirm this fact. We speculate that the increased $TCR_{s\text{-}e}$ after formation cycles might be due to morphology change of the particles in the electrodes and how they contact the separator. It may also result from electrode delamination or microbubbles getting trapped at the separator-electrode interface. It is well-known experimentally that gas is formed inside the cell during aging and cycling[27–29]. A chemical shuttle exists in typical NMC/Graphite Li-ion batteries. If this results from CO_2 being formed at the cathode from oxalate and consumed at the anode by the reverse reaction, one would expect the reaction to happen near the surface of both electrodes and result in the accumulation of gas at both electrodes. The progressive formation of gas bubbles can cause a contact disconnection between the electrodes and the separator[30]. This local delamination leads to areas of dry-out resulting in loss of capacity and regions of high impedance[30–32]. More research is needed to incorporate the effects of cycling into the *TCR* model.

Our results show that the battery total thermal resistance might increase by more than 70% as a result of cycling. While the absolute temperature rise in a battery depends on many factors, some external to the battery, the cell's temperature gradient depends directly on the total thermal resistance. As a result, the peak temperature rise inside a cycled cell during steady state could be 70% higher than expected if estimates are based only on surface temperature measurements and calibrations performed on uncycled cells.

Conclusions

Our measurements reveal that the thermal resistance of a complete lithium-ion battery is dominated by the thermal contact resistances between the separator and both electrodes, and increases during formation cycling. Our theoretical model explains the origin of this high thermal contact resistance, which explains why Li ion batteries' measured thermal resistance is higher than component-based theoretical predictions[8]. We note that while we measured the thermal properties of a single battery "unit cell," this electrode-separator sandwich is repeated dozens of times within the full stack of commercial battery geometries. The $TCR_{s\text{-}e}$ is therefore also repeated dozens of times volumetrically throughout the full cross section of a battery where its deleterious effect on the internal heat transfer is magnified proportionately. As a result, the total thermal resistance of the battery can increase by over 70% during formation cycling. Our analysis indicates that at the separator-electrode interface, most of the heat flows through the liquid electrolyte instead of the solid particles, which means mitigation strategies proposed in the literature such as increasing the carbon loading to increase the thermal conductivity of electrodes[5] will have limited impact. A better strategy will be increasing k of the electrolyte or geometry modification such as decreasing the size of the active particles or increasing the thickness of the electrodes to reduce the $TCR_{s\text{-}e}$ or its relative impact, respectively. For solid electrolytes[33] we expect the situation to be similar to that of the dry electrodes in the current study due to the presence of air gaps, which means the equivalent TCR could be much higher and influenced by the thermal conductivity of the solid particles. These findings have far-reaching design implications for both current generations of batteries based on liquid electrolytes and for future solid electrolyte batteries.

Future research should investigate the changes in particle morphology near the separator and the effects of pouch cell degassing after the formation cycles to assess these candidate causes for the degrading thermal performance. Sensors should be made more robust so that they can survive long past the formation cycles. Fabrication improvements such as parylene adhesion promoters should allow sensors to last up to 100 cycles. *Operando* sensors that last 100+ cycles could yield important insights into how extended battery use affects thermal transport properties and whether the increasing $TCR_{s\text{-}e}$ eventually levels off. Combined with post-mortem analysis (e.g. structural imaging and spectroscopic analysis using XPS), these studies could help uncover the root cause for the worsening $TCR_{s\text{-}e}$ so that it can mitigated, improving battery performance, safety, and lifetime.

Acknowledgments

We thank Chris Jones and Peter Tatum for their help in designing and constructing measurement equipment. **Funding**: This work was supported by the Assistant Secretary for Energy Efficiency and Renewable Energy, Vehicles Technology Office, of the U.S. Department of Energy under Contract No. DEAC02-05CH11231. Work at Molecular Foundry was supported by the Office of Science, Office of Basic Energy Sciences, of the U.S. Department of Energy under Contract No. DE-AC02-05CH11231. **Author Contributions**: Conceptualization and Funding acquisition, RP; Investigation and Formal analysis SL; Methodology, SL lead, SK support; Resources, YF and SK; Supervision, RP lead, VB support; Writing – original draft, SL; Writing – review & editing, SL, RP, SK, and VB. **Competing interests**: The authors declare no competing interests.

References

1. Dunn, B., Kamath, H. & Tarascon, J. Electrical energy storage for the grid: A Battery of choices. *Science (80-.).* **334**, 928–935 (2011).
2. Wang, C. Y. *et al.* Lithium-ion battery structure that self-heats at low temperatures. *Nature* **529**, 515–518 (2016).
3. Bandhauer, T. M., Garimella, S. & Fuller, T. F. A Critical Review of Thermal Issues in Lithium-Ion Batteries. *J. Electrochem. Soc.* **158**, R1 (2011).
4. Palacin, M. R. & de Guibert, A. Why do batteries fail? *Science (80-.).* **351**, 1253292–1253292 (2016).
5. Keyser, M. *et al.* Enabling fast charging – Battery thermal considerations. *J. Power Sources* **367**, 228–236 (2017).
6. Liu, Y., Zhu, Y. & Cui, Y. Challenges and opportunities towards fast-charging battery materials. *Nat. Energy* (2019). doi:10.1038/s41560-019-0405-3
7. Yang, Y., Huang, X., Cao, Z. & Chen, G. Thermally conductive separator with hierarchical nano / microstructures for improving thermal management of batteries. *Nano Energy* **22**, 301–309 (2016).
8. Vishwakarma, V. *et al.* Heat transfer enhancement in a lithium-ion cell through improved material-level thermal transport. *J. Power Sources* **300**, 123–131 (2015).
9. Shah, K., Vishwakarma, V. & Jain, A. Measurement of Multiscale Thermal Transport Phenomena in Li-Ion Cells: A Review. *J. Electrochem. Energy Convers. Storage* **13**, 030801 (2016).
10. Richter, F., Kjelstrup, S., Vie, P. J. S. & Burheim, O. S. Thermal conductivity and internal temperature profiles of Li-ion secondary batteries. *J. Power Sources* **359**, 592–600 (2017).
11. Kantharaj, R. & Marconnet, A. Heat Generation and Thermal Transport in Lithium-Ion Batteries: A Scale-Bridging Perspective. *Nanoscale Microscale Thermophys. Eng.* **23**, 1–29 (2019).
12. Gaitonde, A., Nimmagadda, A. & Marconnet, A. Measurement of interfacial thermal conductance in Lithium ion batteries. *J. Power Sources* **343**, 431–436 (2017).
13. Verma, P., Maire, P. & Novák, P. A review of the features and analyses of the solid electrolyte interphase in Li-ion batteries. *Electrochim. Acta* **55**, 6332–6341 (2010).
14. Cahill, D. G. Thermal conductivity measurement from 30 to 750 K: the 3ω method. *Rev. Sci. Instrum.* **61**, 802–808 (1990).
15. Dames, C. & Chen, G. 1ω, 2ω, and 3ω Methods for Measurements of Thermal Properties. *Rev. Sci. Instrum.* **76**, 124902 (2005).
16. Tong, T. & Majumdar, A. Reexamining the 3-omega technique for thin film thermal characterization. *Rev. Sci. Instrum.* **77**, 104902 (2006).
17. Bauer, M. L. & Norris, P. M. General bidirectional thermal characterization via the 3ω

technique. *Rev. Sci. Instrum.* **85**, 064903 (2014).

18. Borca-Tasciuc, T., Kumar, A. R. & Chen, G. Data reduction in 3ω method for thin-film thermal conductivity determination. *Rev. Sci. Instrum.* **72**, 2139–2147 (2001).

19. Feldman, A. Algorithm for solutions of the thermal diffusion equation in a stratified medium with a modulated heating source. *High Temp. Press.* **31**, 293–298 (1999).

20. Maleki, H., Al-Hallaj, S., Selman, J. R., Dinwiddie, R. B. & Wang, H. Thermal Properties of Lithium-Ion Battery and Components. *J. Electrochem. Soc.* **146**, 947 (1999).

21. Didion, D. A. *An Analysis and Design of A Linear Guarded Cut-Bar Apparatus For Thermal Conductivity Measurements*. (1968).

22. Prasher, R. S. Ultralow thermal conductivity of a packed bed of crystalline nanoparticles: A theoretical study. *Phys. Rev. B - Condens. Matter Mater. Phys.* **74**, 1–5 (2006).

23. Prasher, R. S. & Phelan, P. E. Microscopic and macroscopic thermal contact resistances of pressed mechanical contacts. *J. Appl. Phys.* **100**, 1–8 (2006).

24. Wang, B. X., Zhou, L. P. & Peng, X. F. A fractal model for predicting the effective thermal conductivity of liquid with suspension of nanoparticles. *Int. J. Heat Mass Transf.* **46**, 2665–2672 (2003).

25. Gustafsson, S. E. Transient plane source techniques for thermal conductivity and thermal diffusivity measurements of solid materials. *Rev. Sci. Instrum.* **62**, 797–804 (1991).

26. Monachon, C., Weber, L. & Dames, C. Thermal Boundary Conductance :A Materials Science Perspective. *Annu. Rev. Mater. Res.* **accepted**, (2016).

27. Self, J., Aiken, C. P., Petibon, R. & Dahn, J. R. Survey of Gas Expansion in Li-Ion NMC Pouch Cells. *J. Electrochem. Soc.* **162**, A796–A802 (2015).

28. Xiong, D. J. *et al.* Studies of Gas Generation, Gas Consumption and Impedance Growth in Li-Ion Cells with Carbonate or Fluorinated Electrolytes Using the Pouch Bag Method. *J. Electrochem. Soc.* **164**, A340–A347 (2017).

29. Vetter, J. *et al.* In situ study on CO2 evolution at lithium-ion battery cathodes. *J. Power Sources* **159**, 277–281 (2006).

30. Matadi, B. P. *et al.* Effects of Biphenyl Polymerization on Lithium Deposition in Commercial Graphite/NMC Lithium-Ion Pouch-Cells during Calendar Aging at High Temperature. *J. Electrochem. Soc.* **164**, A1089–A1097 (2017).

31. Mao, Z., Farkhondeh, M., Pritzker, M., Fowler, M. & Chen, Z. Calendar Aging and Gas Generation in Commercial Graphite/NMC-LMO Lithium-Ion Pouch Cell. *J. Electrochem. Soc.* **164**, A3469–A3483 (2017).

32. Jalkanen, K. *et al.* Cycle aging of commercial NMC/graphite pouch cells at different temperatures. *Appl. Energy* **154**, 160–172 (2015).

33. Xu, L. *et al.* Interfaces in Solid-State Lithium Batteries. *Joule* **2**, 1991–2015 (2018).

34. *CRC Handbook of Chemistry and Physics, 90th Edition*. (CRC Press, 2009).

35. Aluminum Oxide, Al2O3 Ceramic Properties. *Accuratus* Available at: http://accuratus.com/alumox.html.

36. *SCS Parylene Properties*. (2007).

37. Chen, S. C., Wan, C. C. & Wang, Y. Y. Thermal analysis of lithium-ion batteries. *J. Power Sources* **140**, 111–124 (2005).

38. Lin, C., Chen, K., Sun, F., Tang, P. & Zhao, H. Research on thermo-physical properties identification and thermal analysis of EV Li-ion battery. in *5th IEEE Vehicle Power and Propulsion Conference, VPPC '09* 1643–1648 (2009). doi:10.1109/VPPC.2009.5289653

39. Vishwakarma, V. & Jain, A. Measurement of in-plane thermal conductivity and heat capacity of separator in Li-ion cells using a transient DC heating method. *J. Power Sources* **272**, 378–385 (2014).

40. *EPO-TEK EK2000 Technical Data Sheet*. (2017).

41. Bougher, T. L. *et al.* Thermal boundary resistance in GaN films measured by time domain thermoreflectance with robust monte carlo uncertainty estimation. *Nanoscale Microscale Thermophys. Eng.* **20**, 22–32 (2016).

42. Ledbetter, H. M. & Naimon, E. R. Elastic Properties of Metals and Alloys. II. Copper. *J. Phys. Chem. Ref. Data* **3**, 897–935 (1974).

43. Qi, Y., Guo, H., Hector, L. G. & Timmons, A. Threefold Increase in the Young's Modulus of Graphite Negative Electrode during Lithium Intercalation. *J. Electrochem. Soc.* **157**, A558 (2010).

44. Wolfenstine, J. *et al.* Mechanical and physical properties of LiNi 0.33 Mn 0.33 Co 0.33 O 2 (NMC). *J. Eur. Ceram. Soc.* **37**, 3213–3217 (2017).

45. Cannarella, J. *et al.* Mechanical Properties of a Battery Separator under Compression and Tension. *J. Electrochem. Soc.* **161**, F3117–F3122 (2014).

Appendix A: Optimization of Sample Design

To optimize our sample we perform extensive sensitivity analyses. The optimized design is given in Figure 2. We define sensitivity in the usual way,

$$S_x^Y = \frac{\partial \ln(Y)}{\partial \ln(x)} = \frac{x_0}{Y_0}\frac{\partial Y}{\partial x} \tag{A1}$$

Where S is the relative sensitivity (dimensionless), Y is the measured signal (in our case either the real or imaginary part of Equation (3)), x is any parameter of Y, and 0 denotes the particular value of Y or x where the sensitivity is being evaluated. The sensitivity tells you how much a relative change in parameter x will change the relative value of the measured signal, Y, and hence how sensitive the measurement is to parameter x. An ideal experiment has high sensitivity to parameters being measured and low sensitivity to all other input parameters (particularly those that are not known to high precision). This results in being able to measure parameter x with high accuracy.

We effectively increase the thickness of the bottom-side electrode current collector to act as a heat sink by attaching an approximately 2 mm thick metal plate of matched material to the bottom electrode current collector. This heat sink draws heat flux from the sensor down through the battery stack to maximize our sensitivity to $TCR_{s\text{-}e}$ without affecting the electrochemical behavior of the cell. It also acts as a heat spreader, rapidly dispersing the thermal wave in-plane and eliminating sensitivity to the outside environment below. Figure 10 shows how the addition of the heat sink boosts the sensitivity to $TCR_{s\text{-}e}$ for both the in-phase and out-of-phase signals.

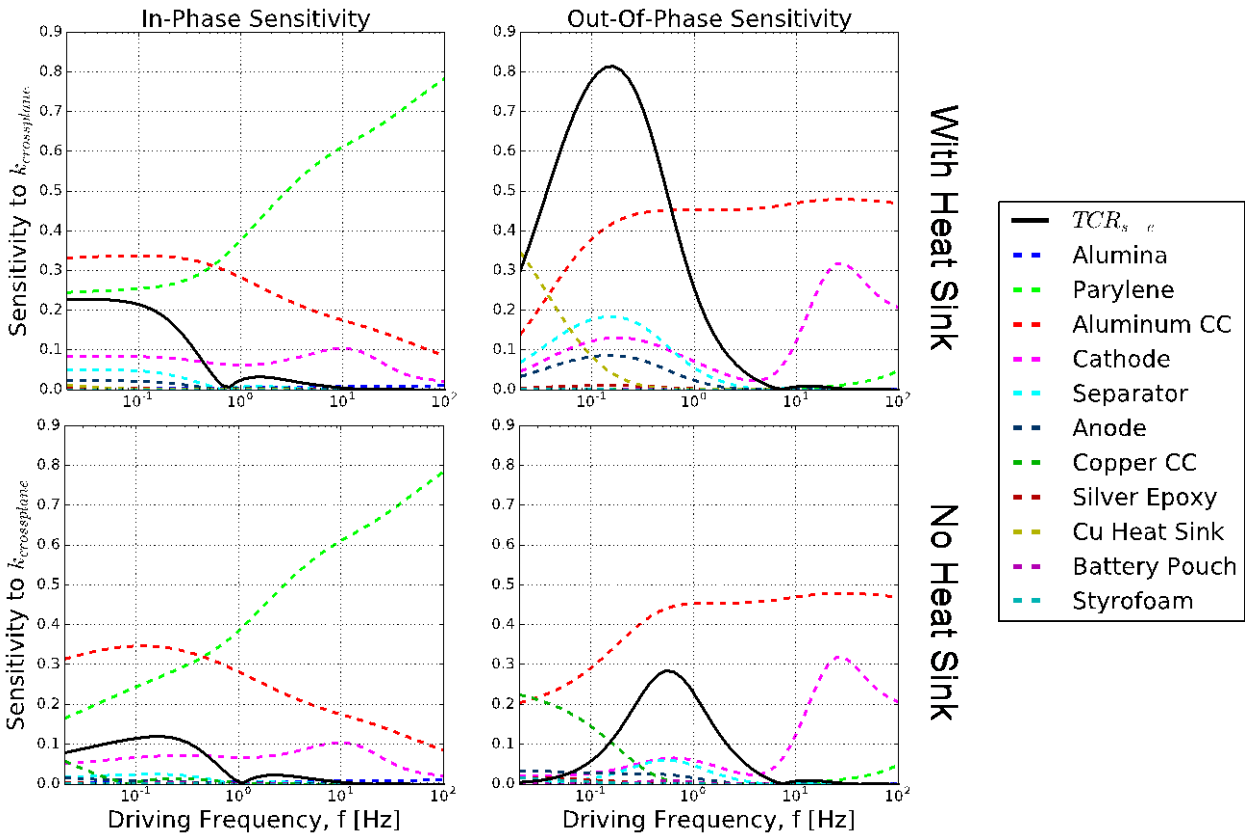

Figure 10. Sensitivity calculation showing impact of adding heat sink. Left column shows the sensitivity of the in-phase data to the thermal conductivity of each layer as a function of electrical current driving frequency. Right column shows the same for the out-of-phase data. Black line indicates the sensitivity to the separator-electrode thermal contact resistance, $TCR_{s\text{-}e}$. For all plots the absolute value of the sensitivity is plotted. Top row shows sensitivity calculations with a heat sink attached to the bottom electrode. Bottom row shows the same calculations without a heat sink.

The heat sink most significantly increases the out-of-phase signal sensitivity to $TCR_{s\text{-}e}$. This means the same relative difference in $TCR_{s\text{-}e}$ will produce a much larger relative change in the measured out-of-phase signal for a sample with a heat sink than one without a heat sink. The in-phase signal gets a larger absolute boost (greater change in absolute rather than relative signal strength as measured in volts for a given relative change in $TCR_{s\text{-}e}$), as shown in Figure 11. Figure 10 also shows that the only other parameters in the battery that have a sensitivity greater

than the $TCR_{s\text{-}e}$ are the parylene and the aluminum current collector. Therefore the aluminum properties are among the dominant sources of uncertainty in our measured $TCR_{s\text{-}e}$ values. Fortunately, the aluminum current collector, simply being aluminum foil, has well known properties that can be taken from literature. The parylene thermal resistance is the second parameter that we fit in our two-parameter fit (discussed in detail in Appendix C: 3-Omega Measurements and Data Analysis), and is found to vary by 2% to 7% (std) among all measurements for each individual sample. Sensitivities to heat capacities and in-plane thermal conductivities are less than the cross-plane thermal conductivity sensitivities. Sensitivity to layer thicknesses are often roughly the same as the negative of the cross-plane k sensitivities, because for many layers the measurement is sensitive to L/k. These other sensitivities are therefore omitted from the plot to reduce visual clutter.

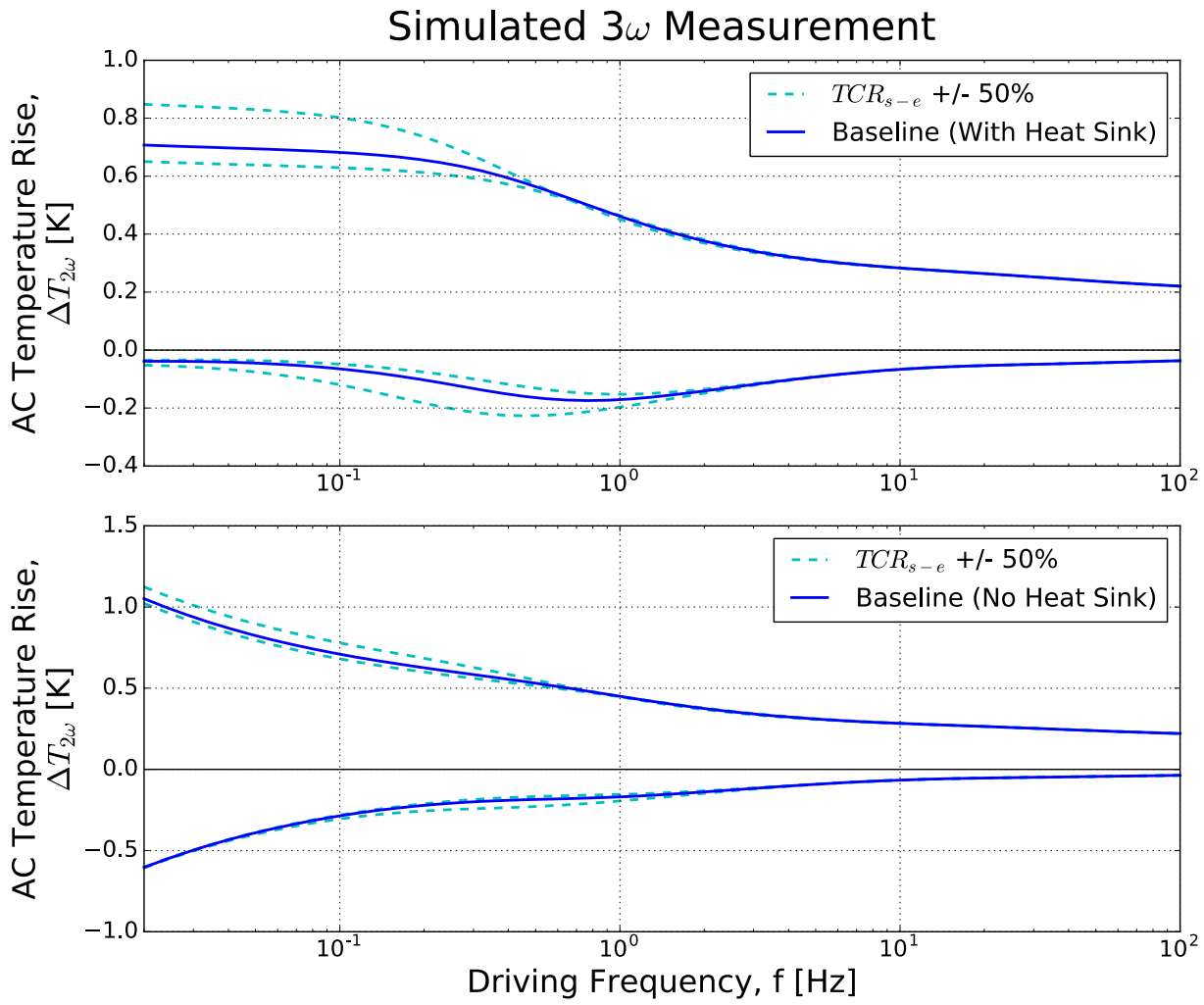

Figure 11. Simulated 3ω measurement with and without a heat sink. Solid blue lines show the in-phase (positive) and out-of-phase (negative) baseline temperature response to periodic heating. Dashed light blue lines illustrate the sensitivity to the separator-electrode thermal contact resistance, $TCR_{s\text{-}e}$, by perturbing it by +/- 50%. The top plot assumes there is a heat sink attached to the bottom electrode. The bottom plot assumes there is no heat sink.

We also added a 3 mm thick layer of 2 lb cross-linked closed cell polyethylene foam (electrolyte-compatible) on top of the sensors (see Figure 2). The foam prevents parasitic heat leakage from the sensors, shields the sensors from electrolyte, and distributes downward pressure uniformly. We measured k_{foam} = 0.038 W/m-K using the TPS Hot Disk previously mentioned.

The frequency-dependent thermal resistance of this foam layer is 100 to 200 times higher than the combined frequency-dependent thermal resistance of the battery stack below the sensor for all measurement frequencies. Therefore, less than 1% of the heat produced from the sensor is parasitically lost in the upward direction through the foam and layers above it. We therefore use a single-directional 3ω thermal model.

Finally, we place a 3 mm thick layer of Styrofoam underneath the battery pouch cell (Figure 2) to make the measurements thermally insensitive to the external environment regardless of the environment properties. We measured $k_{styrofoam}$ = 0.024 W/m-K using the TPS Hot Disk previously mentioned.

Appendix B: Sample Fabrication

Electrodes and electrolyte used had the following compositions:

- *Anode*: 89 wt% graphite, 3 wt% acetylene black, and 8 wt% PVDF polymer binder
- *Cathode*: 92.8 wt% $LiNi_{1/3}Mn_{1/3}Co_{1/3}O_2$ (NMC), 3.2 wt% acetylene black, and 4 wt% PVDF polymer binder
- *Electrolyte*: 1 Molar $LiPF_6$ salt concentration dissolved in 50 wt% ethylene carbonate (EC) and 50 wt% diethyl carbonate (DEC)

Cathodes and Anodes were fabricated in-house. The active material, acetylene black, and PVDF were mixed with N-methyl-2-pyrrolidone using a Polytron PT 10-35 homogenizer at 3000 rpm to form a uniform, viscous slurry. Then the slurry was coated on 20 micron Al or 17 micron Cu foil current collectors and was dried overnight naturally.

Separators (Celgard 2400), electrolyte, and all other pouch cell materials (e.g. pouch, tabs) were purchased from *MTI Corp*. and are industry standard. Assembled pouch cells had capacities of around 25 mAh.

The entire multilayered battery stack with additional sample support layers is shown in Figure 2. Fully fabricated electrodes were first coated in approximately 500 nm of parylene on their current collector side. This formed a conformal and flexible dielectric layer to electrically insulate the 3ω sensors from the current collector. An additional 100 nm of Al_2O_3 was deposited via atomic layer deposition (ALD) on top of the parylene to fill in any pinholes and serve as a more favorable deposition surface for the metallic sensors.

The 3ω sensors were then deposited on top of the insulation layer through a shadow mask using thermal evaporation. First a 10 nm Cr adhesion layer was deposited, followed by approximately 300 nm of Au to form the sensors themselves. The main heater line in the 3ω sensors was 3 mm long x 100 microns wide, with current and voltage probe connector traces designed to not distort the intended heater line isotherm shapes.

We attached 50 micron diameter electrically insulated copper wires to 3ω sensor contact pads via an electrically conducting silver epoxy, cured at 130 °C for 20 minutes. After sensor temperature coefficient of resistance (α) calibrations, we attached 3 mm thick slabs of 2 lb cross-linked closed cell polyethylene foam directly on top of the sensors. We formed a watertight seal between the foam and electrodes via a ring of *Torr Seal* epoxy around the perimeter of the electrode top surface. The foam prevents parasitic heat leakage from the sensors, shields the sensors from electrolyte, and distributes downward pressure uniformly. Pressure paper tests were performed to ensure that applied pressure is uniformly distributed across the battery and not concentrated around the perimeter.

Each battery has sensors only on one side. On the backside electrode (without sensors) we attach a 2 mm thick highly thermally conducting metal plate of matched material to the current collector (i.e. Cu). The plate is attached using a layer of highly thermally conducting silver

epoxy, approximately 50 microns thick. This plate acts as an AC heat sink to draw heat flux through the battery stack and maximize our sensitivity without affecting the electrochemical behavior of the cell. It also acts as a heat spreader, rapidly dispersing the thermal wave in-plane and eliminating sensitivity to the outside environment below. To fully isolate our signal from the outside environment below, a 3 mm thick layer of Styrofoam is placed below the battery outside of the pouch during measurements.

Inside a glove box, the full battery stack (foam-sensors-cathode-separator-anode-heat sink) is hermetically sealed within a pouch with electrolyte (Figure 1(B)). The wires for the 3ω sensors and the tabs used for accessing the battery are both accessible from outside the pouch. The sensors are entirely electrically isolated from the battery. All materials used within the battery (epoxies, foam, etc.) have verified compatibility with the electrolyte. Due to low yield, multiple sensors were deposited and wired up for each electrode. Typically only zero or one sensor would survive the entire fabrication and pouch cell assembly process.

Appendix C: 3-Omega Measurements and Data Analysis

Measurement Protocol: The 3ω sensors are powered using a Keithley 6221 AC Current source. Sensors typically had a resistance of approximately 15 Ohms, and were driven by approximately 25 mA RMS of current. This resulted in approximately 1 K of AC temperature rise at the battery surface. We drove the sensors at frequencies ranging from 20 mHz to 100 Hz, corresponding to thermal penetration depths of a couple tens of microns to a couple mm, spanning the full thickness of the battery sample. The resulting third harmonic voltage response was measured using an Amtek 7270 Lock-in Amplifier referenced to the current source. As is standard practice for 3ω, we subtracted a pure 1ω "dummy signal" from the measured signal using the Lock-in's

differential input in order to isolate the significantly smaller magnitude 3ω component that we wish to measure. We generate this pure 1ω dummy signal using a large thermal mass low α resistor matched to the electrical resistance of the sensor and connected in series with the same driving current. We use lock-in time constants between 0.2 seconds and 50 seconds, corresponding to equivalent noise bandwidths of 0.83 Hz to 0.003 Hz. As a result, our 3ω measurements had signal-to-noise ratios (SNR) of 10 to 10^3 for the out-of-phase signal, and 10^2 to 10^4 for the in-phase signal. This means no significant noise resulting from thermal or electrical signals generated by the environment or the operation of the cycling battery itself influence our measurement. We only detect signals at precisely the frequency at which we are driving the 3ω sensor.

We calibrate the temperature coefficient of electrical resistance, $\alpha = \frac{1}{R_0}\frac{dR}{dT}$, individually for each sensor, where R_0 [Ohms] is the electrical resistance at the temperature T = 0 °C by convention. For each of 5 temperatures spanning a total of approximately 40 K we measured the electrical resistance of the sensor using a 4-point electrical probe configuration. To avoid temperature ambiguity from the self-heating of the sensor during measurement a series of resistance measurements are performed at 5 different currents at each temperature. From these, we extrapolate the electrical resistance in the limit of zero current from the intercept, often referred to as the "cold wire" resistance, for each temperature. We fit a line to the resulting Resistance-vs-Temperature plot, having a typical $R^2 \sim 0.9999$. We extract α from this plot. We were able to perform a post-mortem analysis on our oldest battery sample (#2), and re-measure α of the sensor using an electrical probe station in spite of the original sensor connections being

broken. After all handling, battery cycles, and 3ω measurements, and then sitting dormant in a drawer for over a year with electrolyte, α had only decreased by 6.1%.

For cycling, a battery pouch cell is placed inside a metal battery cycling chamber actively maintained at 25 °C with a weight on top of the battery providing approximately 5 PSI of downward pressure. A layer of 3 mm thick Styrofoam is placed underneath the battery outside the pouch to thermally isolate the sample from the below environment. Constant current is used to cycle the battery slowly for the formation cycles at rates of C/20 to C/10 for 1 to 2 weeks while we perform intermittent 3ω measurements during and between charging and discharging cycles.

Data Analysis: We measure thermal transport properties by least squares fitting of Equation (3) to the measured third harmonic of the complex voltage response. We simultaneously fit the same parameter set to the in-phase and out-of-phase components of the 3ω data. Physically, this refers to the periodic surface temperature response being in or out of temporal phase with the periodic driving heat flux and mathematically corresponds to the real and imaginary components of the complex temperature, respectively, given above in Equation (2). The thermophysical properties of all layers both inside and outside of the battery used for data fitting are given in Table 1.

	Wet Layer Properties (with electrolyte)			**Dry Layer Properties (without electrolyte)**		
	$k_{cross\text{-}plane}$ **(W/m-K)**	C **(kJ/m^3-K)**	L **(microns)**	$k_{cross\text{-}plane}$ **(W/m-K)**	C **(kJ/m^3-K)**	L **(µm)**
Alumina	17 [34,35]	3080 [35]	0.1*	same as wet	same as wet	same as wet

Parylene	0.1 to 0.2*	960 [36]	0.4 to 0.8*	same as wet	same as wet	same as wet
Al foil	237 [34]	2420 [34]	20*	same as wet	same as wet	same as wet
Cathode	0.828*	3510 [5]	65 to 72*	0.548*	2540[c]	same as wet
Separator	0.3 [5,10,37,38]	2180 [5,37–39]	26*	0.11 [10]	1400[c]	same as wet
Anode	1.44*	2030 [5,37]	52 to 57*	1.05*	9020[c]	same as wet
Cu foil	401 [34]	3440 [34]	17*	same as wet	same as wet	same as wet
Ag Epoxy	10 [40]	2000[g]	50[g]	same as wet	same as wet	same as wet
Cu Heat Sink	same as foil	same as foil	2000*	same as wet	same as wet	same as wet
Battery Pouch	0.33[d]	2000[g]	111*	same as wet	same as wet	same as wet
Styrofoam	0.024*	16*	3000*	same as wet	same as wet	same as wet

* Measured in-house by this paper's authors
[c] Calculated based on corresponding wet values, porosity, and electrolyte properties
[g] Best guess value, and shown to have negligible influence on results
[d] Calculated from series thermal resistance model based on manufacturer-specified material layer stack.

Table 1. Thermophysical properties of each layer in the battery 3ω model used for data fitting. Unless otherwise indicated, properties are the average of values taken from the associated references. Uncertainties are given in **Table 2**.

Our 3ω thermal model accounts for the finite heater line width and full anisotropic multilayer geometry of the battery. Our model takes as input the cross-plane thermal conductivity, heat capacity, and thickness of each layer. All properties used for all layers in data fitting are given in Table 1. Unless otherwise indicated, properties are taken from the adjacent listed references (if more than one reference is given, the average value from all listed references is used). A range of values indicates this property varies from sample to sample. The anode and cathode active materials were taken to have a thermal conductivity anisotropy ratio (in-

plane/cross-plane) of 11.9 and 18.6 respectively[5], although these two parameters had negligible impact on data fitting. Electrolyte, Polyethylene foam, and Styrofoam thermal conductivities and heat capacities were measured in-house using a commercial 2200 Hot Disk purchased from *Thermtest* based on the transient plane source technique[25]. All thicknesses are measured using a micrometer.

We simultaneously fit two free parameters in the model. The first fitted parameter is the unknown thermal resistance of the parylene electrical insulation layer, $R_{parylene} = L_{parylene}/k_{parylene}$, and the second parameter is the total thermal contact resistance of the two separator-electrode interfaces, $TCR_{s\text{-}e}$ (i.e. $TCR_{s\text{-}e} = TCR_{separator\text{-}cathode} + TCR_{separator\text{-}anode}$). These two parameters affect the model in qualitatively different ways and can be robustly fit simultaneously. We fit $R_{parylene}$ because it varies by up to a factor of 2 based on deposition conditions and we have a very high sensitivity to this parameter due to its adjacency to the sensor. There was a 2% standard deviation among all seven fitted values of $R_{parylene}$ corresponding to the seven dry and wet 3-omega measurements for battery 1. The standard deviation among the eight fitted $R_{parylene}$ values for battery 2 was 7%. These standard deviations are within the predicted uncertainty for this parameter, consistent with a constant valued $R_{parylene}$ as is expected of multiple measurements from the same sample. During the fit we apply a constraint requiring the separator-anode and separator-cathode *TCR*s to be equal in magnitude, and then simultaneously fit this value as a single parameter. This decision is made based on our TCR model, corroborated by our *ex-situ* Cut Bar measurements, showing that these two interfaces have comparable *TCR*s. We also confirm that for all of the data the same total value of $TCR_{s\text{-}e}$ is obtained to better than 1% regardless of whether during the fitting procedure it is all attributed to the separator-anode interface, the separator-cathode interface, or any splitting ratio between the

two ranging from 100:1 to 1:100. As is standard practice for these kinds of multilayer analytical models, interfaces are modeled as layers with vanishing thickness (1 nm) and heat capacity (10^{-3} kJ/m^3-K). We fit the *TCR* of an interface by fitting its cross-plane thermal conductivity, with the corresponding *TCR* given by $TCR = L/k$ [m^2-K/W], where L is the 1 nm thickness.

Appendix D: Statistical Analysis

Monte Carlo Simulations: Values and error bars of the main results (Figure 5(B)) are calculated using a Monte Carlo (MC) simulation approach based on Ref[41], except we use a more conservative 95% confidence interval instead of the 80% confidence interval (i.e. 90th/10th percentile bounds) used in the reference. The results of our MC simulation for a representative 3-Omega measurement are shown in Figure 12. After 500 MC trials the relative change in fitted values with additional trials drops to 0.1%. In order to make sure all results are rigorously converged, we run ~3000 trials for each measurement, resulting in an average relative change <0.01% from additional trials.

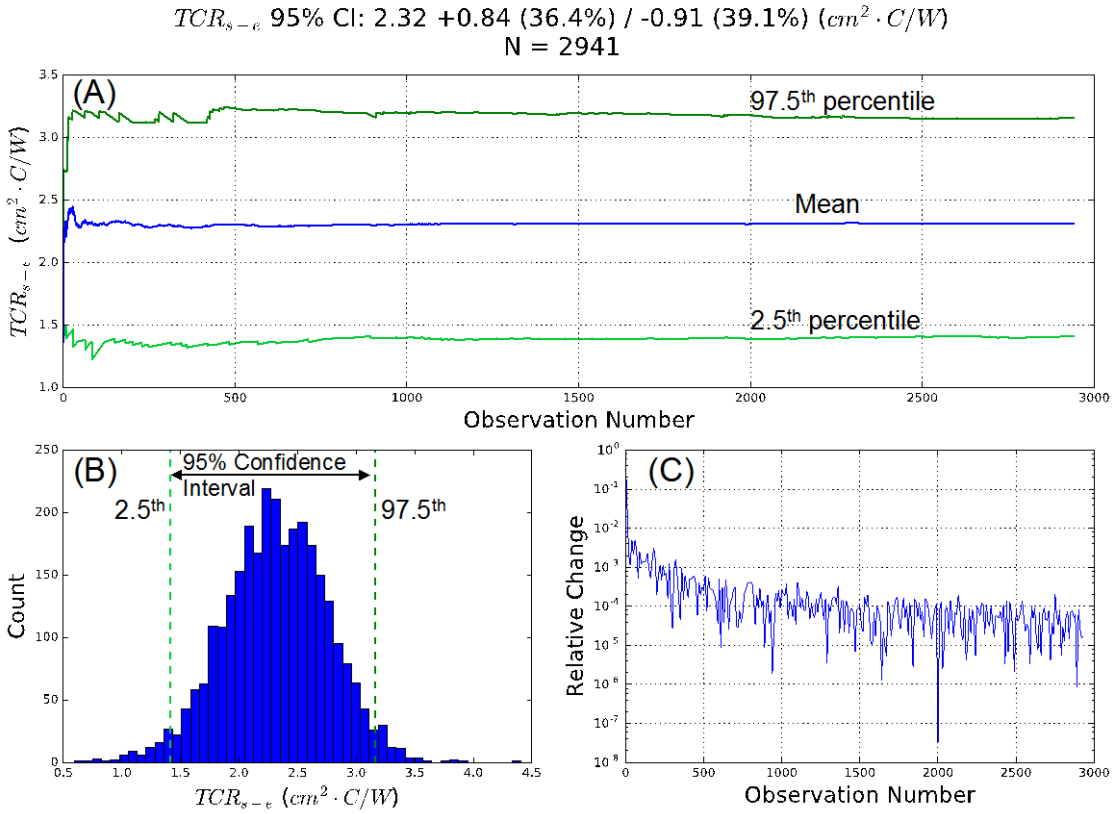

Figure 12. Representative results of Monte Carlo simulation for one 3-Omega measurement. (A) Convergence of MC simulation. (B) Histogram of best-fit values for $TCR_{s\text{-}e}$ for one 3-Omega measurement, with 95% confidence interval bounds shown. (C) Relative change in cumulative mean as additional MC trials are performed.

The uncertainties for all input parameters within the full layer stack used in the MC simulation are given in Table 2. In addition to the uncertainties of these layers, we incorporated the following parameter uncertainties: the measured electrical resistance of the heater line, R_e (uncertainty calculated from each measurement), the calibrated temperature dependence of the heater line's electrical resistance, dR_e/dT (6.1%, post-mortem measurement), the heater line width (20%, measured), and the heater line length (1.7%, measured). Other uncertainties including the thermal conductivity anisotropy ratio of anode and cathode, and the electrical

currents and voltages, had a negligible impact on any fitted parameter (due to those input parameters' low sensitivities and/or small absolute uncertainties).

	Wet Layer Uncertainties (i.e. with electrolyte)			Dry Layer Uncertainties		
	kz	***C***	***L***	***kz***	***C***	***L***
Alumina	5.9%[d]	6.5%[d]	5.0%[g]	same as wet	same as wet	same as wet
Parylene	Based on fit	18%[d]	Based on fit	same as wet	same as wet	same as wet
Al foil	5.0%[g]	5.0%[g]	10%*	same as wet	same as wet	same as wet
Cathode	22%*	10%[d]	4.6%*	1.8%*	13%[c]	same as wet
Separator	19%[d]	6.0%[d]	3.8%*	23%[d]	12%[c]	same as wet
Anode	9.0%*	6.3%[d]	10%[d]	7.6%*	12%[c]	same as wet
Cu foil	5.0%[g]	5.0%[g]	2.9%*	same as wet	same as wet	same as wet
Ag Epoxy	30%[d]	50%[g]	50%[g]	same as wet	same as wet	same as wet
Cu Heat Sink	same as foil	same as foil	10%*	same as wet	same as wet	same as wet
Battery Pouch	20%[g]	50%[g]	0.9%*	same as wet	same as wet	same as wet
Styrofoam	10%*	20%*	N/A	same as wet	same as wet	same as wet

* Measured in-house by this paper's authors
[c] Calculated based on corresponding wet values, porosity, and electrolyte properties
[g] Best guess value
[d] From source or from calculated standard deviations among corresponding literature values

Table 2. Uncertainties (one standard deviation) in thermophysical properties of each layer in the battery 3ω model used for data fitting. All values are either based on repeated measurements by the authors, calculated standard deviations among the same literature values used to calculate properties in **Table 1**, or best estimates. Anode thickness uncertainty is increased to reflect possible swelling during cycling.

The dominant sources of uncertainty for the dry $TCR_{s\text{-}e}$ were the temperature coefficient of resistance, the thickness of the Al current collector, $k_{separator}$, and k_{Al}. For the wet contact, the dominant sources of uncertainty were the same as for the dry contact plus $k_{cathode}$, because our *ex-situ* measurement uncertainty for $k_{cathode}$ was much higher for the wet cathode than for the dry cathode.

Statistical Hypothesis Testing: In this section we discuss the formal hypothesis testing of all major claims of the paper, demonstrating their statistical significance.

To evaluate the claim that the $TCR_{s\text{-}e}$ gets worse with cycling, we use linear regression to fit a line to the $TCR_{s\text{-}e}$ versus cycle number data in Figure 5(B) for all measurements that include electrolyte. We set a significance level of 0.05 and test the null hypothesis that such a line has a slope of zero, indicating there is no trend of $TCR_{s\text{-}e}$ as a function of battery cycling. Using Python's *scipy.stats.linregress* method, we calculate p-values of $p_1 = 0.029$ for battery sample 1 and $p_2 = 0.012$ for battery sample 2. Therefore, we reject the null hypothesis of no relationship between cycle number and $TCR_{s\text{-}e}$ assuming significance level 0.05, and conclude that $TCR_{s\text{-}e}$ does increase with cycle number. Because battery samples 1 and 2 are independent samples with independent measurements, the experiment's combined p-value is $(p_1)(p_2) = p = 0.00035$. If $TCR_{s\text{-}e}$ did not vary with cycle number, then the probability of obtaining measurements at least as extreme as our data for both samples is less than 0.035%.

Because the 95% confidence intervals constructed for the dry (no electrolyte) and wet (with electrolyte, before cycling) measurements do not overlap for each sample, we reject the null hypothesis that the mean $TCR_{s\text{-}e}$ does not change with the addition of electrolyte. We therefore conclude that adding electrolyte reduces $TCR_{s\text{-}e}$.

Because the 95% confidence intervals constructed for all mean $TCR_{s\text{-}e}$ measurements lie entirely above the value $TCR_{s\text{-}e}$ = 0 cm^2-C/W, we reject the null hypothesis that the $TCR_{s\text{-}e}$ does not increase the overall thermal resistance of the battery. We therefore conclude that the $TCR_{s\text{-}e}$ increases the battery's overall thermal resistance. The expected values of the $TCR_{s\text{-}e}$ are given by the MC means, as reported in Figure 5(B).

Appendix E: Thermophysical Properties for Thermal Contact Resistance Model

The thermophysical properties used in evaluating the TCR model for both anodes and cathodes in contact with separators and copper cut bars are given in Table 3.

	Young's Modulus (Gpa)	Poisson's Ratio	*k* (W/m-K)
Copper	124 [42]	0.35 [42]	401[s]
Anode Particles (Graphite)	32 [43]	0.32 [43]	5.8[c]
Cathode Particles (NMC)	199 [44]	0.25 [44]	2.3[c]
Dry Separator	0.21 [45]	0.35[g]	0.11[s]
Wet Separator	0.18 [45]	0.35[g]	0.3[s]
Electrolyte	N/A	N/A	0.2*

* Measured in-house by this paper's authors using Hot Disk
[c] Calculated based on the Bruggeman model [24]
[s] Same values and references as listed in Table 1.
[g] Best guess value, and shown to have negligible influence on results

Table 3. Thermophysical properties of each material used for the *TCR* model. Unless otherwise indicated, properties are taken from the associated references.